

Magnetized Rotating Isothermal Winds

Matthias J. Raives^{1,2,3*}, Matthew S. B. Coleman^{4,5}, & Todd A. Thompson^{2,3,6}

¹*The Observatories of the Carnegie Institution for Science, 813 Santa Barbara St., Pasadena, CA 91101, USA;*

²*Department of Astronomy, The Ohio State University, Columbus, OH 43210, USA*

³*Center for Cosmology and Astroparticle Physics, The Ohio State University, Columbus, OH 43210, USA*

⁴*Department of Astrophysical Sciences, 4 Ivy Lane, Princeton University, Princeton, NJ 08540, USA*

⁵*Department of Physics and Engineering Physics, Stevens Institute of Technology, Castle Point on the Hudson, Hoboken, NJ 07030, USA*

⁶*Department of Physics, The Ohio State University, Columbus, OH 43210, USA*

1 November 2023

ABSTRACT

We consider the general problem of a Parker-type non-relativistic isothermal wind from a rotating and magnetic star. Using the magnetohydrodynamics (MHD) code Athena++, we construct an array of simulations in the stellar rotation rate Ω_* and the isothermal sound speed c_T , and calculate the mass, angular momentum, and energy loss rates across this parameter space. We also briefly consider the three dimensional case, with misaligned magnetic and rotation axes. We discuss applications of our results to the spindown of normal stars, highly-irradiated exoplanets, and to nascent highly-magnetic and rapidly-rotating neutron stars born in massive star core collapse.

Key words: Stars – Magnetars – Neutron Stars – Winds

1 INTRODUCTION

The spindown of stars¹ as a result of the torque caused by their thermal magnetocentrifugal winds is a classic topic with connections throughout astrophysics. Strong magnetic fields force the wind to effectively co-rotate with the star out to the Alfvén radius R_A , where the poloidal kinetic energy density is approximately equal to the magnetic energy density. By forcing the wind to co-rotate with the star out to large radii, thermal magnetocentrifugal winds can quickly shed large amounts of angular momentum, resulting in rapid spindown.

This problem goes back at least to Schatzman (1962) and Weber & Davis (1967), who investigated the physics of a spherically symmetric magnetized wind, following the classic work by Parker (1958). Sakurai (1985) and Mestel & Spruit (1987) later investigated the problem in two dimensions. Magnetocentrifugal braking is invoked in many astrophysical contexts to explain high energy winds and rapid rotational braking of not only stars, but also disks (e.g., Blandford & Payne 1982). This problem has been investigated most thoroughly in the context of stellar winds, both thermal (Keppens & Goedbloed 2000; Vidotto et al. 2014) and line-driven (ud Doula & Owocki 2002). 3D magnetohydrodynamic (MHD) simulations of the Sun’s corona and the solar wind go back decades (Suess et al. 1977; Suess et al. 1999; Lionello et al. 2001, 2009; Gressl et al. 2014; Reiss et al. 2016), though most such models are calibrated

to the specific conditions of the Sun. Finley & Matt (2017, 2018) have also investigated this problem in the case of magnetized winds with higher-order multipole structure. Magnetocentrifugal braking is also important in discussions of gyrochronology (van Saders et al. 2016), and magnetocentrifugal winds have also been invoked in discussion of hot Jupiter atmospheres (Owen & Adams 2014).

The discussion of stellar spindown also intersects with discussion of proto-neutron star (PNS) and proto-magnetar winds, and the magnetocentrifugal explosion mechanism for core-collapse supernovae (CCSNe). In a core-collapse supernova, after the shockwave is revived and driven outwards into the surrounding massive star progenitor, the cooling PNS core drives a wind into the post-supernova-shock environment (Woosley et al. 1994; Janka & Müller 1995; Burrows et al. 1995). The physics of thermal and purely hydrodynamic (i.e., non-magnetized) winds from PNSs was first explored in Duncan et al. (1986), who considered them in spherical symmetry (1D). Interest in this phase of evolution was piqued by Woosley et al. (1994), who found that their thermodynamic conditions might be conducive to the r -process, though later studies (Qian & Woosley 1996; Hoffman et al. 1997; Otsuki et al. 2000; Thompson et al. 2001; Wanajo et al. 2001) showed that normal PNS winds do not enter a thermodynamic regime conducive to production of the heaviest r -process elements unless they are strongly magnetized (see Thompson 2003; Thompson & ud Doula 2018). Later 1D studies (Thompson et al. 2004; Metzger et al. 2007) considered the effects of magnetic fields on PNS winds, and showed that magnetar strength ($B_* \sim 10^{15}$ G) magnetic fields would dynamically dominate the winds on second-long timescales after explosion (Thompson & Murray 2001), driving them to ener-

* E-mail: mraives@carnegiescience.edu

¹ For simplicity, we use “star” throughout this paper to refer to a generic central body.

gies comparable to gamma-ray bursts (GRBs) and superluminous supernovae (SLSNe). The connection to GRBs has been further explored in Thompson et al. (2004); Thompson (2007); Bucciantini et al. (2009); Metzger et al. (2011), and the SLSNe connection in Wheeler et al. (2000); Komissarov & Barkov (2007); Kasen & Bildsten (2010); Woosley (2010); Dong et al. (2016); Chatzopoulos et al. (2016). Some models also link magnetocentrifugal braking to ordinary (i.e., not superluminous) CCSNe (Ostriker & Gunn 1971; Symbalisty 1984; Sukhbold & Thompson 2017), in addition to other magnetohydrodynamic effects, such as the magnetorotational instability (Akiyama et al. 2003; Thompson et al. 2005; Nishimura et al. 2017).

Despite the broad reach of this problem, there are still key insights missing from the literature. First, most studies of this problem restrict to a narrow range of parameter space. Second, while 2D simulations of this magnetocentrifugal winds are becoming more common (Bucciantini et al. 2006; Finley & Matt 2017), 3D simulations are still relatively new (e.g., Vurm & Metzger 2021, but see, e.g., Vidotto 2009 in the stellar context), and few of them model the effects of magnetospheres not aligned with the axis of rotation (e.g., Subramanian et al. 2022). This paper is an effort to fill in these gaps. We present MHD simulations of 2D and 3D, non-relativistic, magnetocentrifugal winds, using an isothermal equation of state (EOS). While the isothermal EOS is limiting, it also allows us to simultaneously compare these results to existing results in the literature of stellar winds and highly-irradiated “hot Jupiter” winds, in addition to proto-magnetar winds.

In §2, we present details of our simulations, including the initial and boundary conditions used, as well as the details of the rotating reference frame. In §3, we present our findings: how the eigenvalues of the problem – the mass loss rate \dot{M} and the angular momentum loss rate \dot{J} – scale with the various simulation parameters. In particular, we construct a parameter space covering a wide range of rotation rates and sound speeds at a representative magnetic field strength. In §4, we consider our results in the context of proto-magnetar winds, as well as in the context of sun-like stars and irradiated hot Jupiters. Finally, in §5, we discuss our findings in the context of the field and identify areas for future investigation.

2 METHODS

We perform MHD simulations in *Athena++* (Stone et al. 2019), which we have configured to solve the isothermal MHD equations:

$$\frac{\partial \rho}{\partial t} + \nabla \cdot (\rho \mathbf{v}) = 0 \quad (1)$$

$$\frac{\partial \rho \mathbf{v}}{\partial t} + \nabla \cdot \left[\rho \mathbf{v} \mathbf{v} + \left(\rho c_T^2 + \frac{B^2}{2} \right) \mathbf{I} - \mathbf{B} \mathbf{B} \right] = -\rho \nabla \varphi \quad (2)$$

$$\frac{\partial \mathbf{B}}{\partial t} - \nabla \times (\mathbf{v} \times \mathbf{B}) = 0, \quad (3)$$

where φ is the gravitational potential, which we assume to be the point mass potential of the star:

$$\varphi = \frac{GM_*}{r}, \quad (4)$$

and c_T is the isothermal sound speed.

2.1 Rotating Reference Frame

We perform our simulations in the rotating reference frame, i.e., a reference frame where

$$\phi \rightarrow \phi' + \Omega_* t' \quad (5)$$

and

$$\mathbf{v} \rightarrow \mathbf{v}' + \boldsymbol{\Omega}_* \times \mathbf{r}', \quad (6)$$

where $\boldsymbol{\Omega}_* = \Omega_* \hat{\mathbf{z}}$ is the angular velocity of the frame. By construction, this is equal to the (inertial frame) angular velocity of the fluid at $r = R_*$ (see the following section).

Here (and throughout), primed quantities refer to values measured in the rotating reference frame, and unprimed quantities refer to values measured in the inertial (lab) frame. Though r , θ and t do not change between reference frames, we still denote them with primes when measuring quantities in the rotating frame, for the sake of clarity and accuracy.

Since the rotating reference frame is non-inertial, the momentum equation (Equation 2) must be changed to account for the pseudo-forces arising from measurement in this frame. These forces are the familiar Coriolis and centrifugal forces (since $\boldsymbol{\Omega}_* = 0$, the Euler force is zero):

$$\mathbf{a}'_{\text{cor}} = -2\boldsymbol{\Omega}_* \times \mathbf{v}' \quad (7)$$

$$\mathbf{a}'_{\text{cen}} = -\boldsymbol{\Omega}_* \times (\boldsymbol{\Omega}_* \times \mathbf{r}'). \quad (8)$$

We discuss the mathematics of the rotating reference frame, and its implementation in *Athena++*, in more detail in Appendix A.

2.2 Initial Conditions

We initialize all simulations with the density field in spherically-symmetric hydrostatic equilibrium, with the central density, core mass, and core radius normalized to

$$\rho_* = 1 \quad (9)$$

$$GM_* = 1 \quad (10)$$

$$R_* = 1. \quad (11)$$

We initialize the velocity field as a pure radial field plus an angular-momentum conserving angular velocity field. The initial radial velocity is chosen such that it increases slowly at large radii and has a finite value at $r = R_*$. Our chosen velocity field relaxes to the “correct” radial velocity field during an early, transient phase of the simulation. The initial velocity field is

$$\mathbf{v} = 2c_T \left(\frac{r}{r_s} \right)^{1/2} \hat{\mathbf{r}} + \boldsymbol{\Omega} \times \mathbf{r}, \quad (12)$$

where $\boldsymbol{\Omega}$ is the angular velocity profile

$$\boldsymbol{\Omega} = \Omega_* \left(\frac{R_*}{r} \right)^2 \hat{\mathbf{z}}, \quad (13)$$

r_s is the sonic radius (for a non-rotating, non-magnetic isothermal wind)

$$r_s = \frac{GM}{2c_T^2}, \quad (14)$$

and Ω_* is the angular velocity at $r = R_*$. In the rotating reference frame, this becomes

$$\mathbf{v}' = 2c_T \left(\frac{r'}{r_s} \right)^{1/2} \hat{\mathbf{r}}' + (\boldsymbol{\Omega} - \boldsymbol{\Omega}_*) \times \mathbf{r}'. \quad (15)$$

We note that our results are not very sensitive to the initial radial velocity profile, so long as the sonic point is on the grid (i.e., $v_r(R_*) < c_T$ and $v_r(R_{\max}) > c_T$).

We initialize the magnetic field as a dipole field, specified by the vector potential

$$\mathbf{A} = \frac{B_* R_*^3}{2 r^2} \begin{pmatrix} 0 \\ -\sin \alpha \sin \phi \\ \cos \alpha \sin \theta - \cos \theta \cos \phi \sin \alpha \end{pmatrix}, \quad (16)$$

where B_* is the magnetic field strength at the pole at $r = R_*$ and α is the angle between the the rotational axis and magnetic axis. That is,

$$\alpha \equiv \arccos \left(\frac{\mathbf{m} \cdot \boldsymbol{\Omega}_*}{m \Omega_*} \right), \quad (17)$$

where \mathbf{m} is the magnetic dipole moment. The plane defined by these two vectors is the $\phi = 0$ plane. The tilted dipole is discussed in more detail in §3.4 and Appendix B. We also note that, because our calculations are non-relativistic, we can assume $\mathbf{B}' = \mathbf{B}$.

Thus, there are four free parameters we must specify: the sound speed c_T , the tilt angle α , the polar magnetic field strength B_* , and the core angular velocity Ω_* . The field strength is set by the dimensionless parameter

$$\xi_B \equiv \frac{v_A}{v_{\text{esc}}} \Big|_{R_*} = \left(\frac{B_*^2 R_*}{8\pi G M_* \rho_*} \right)^{1/2}, \quad (18)$$

the core angular velocity is specified by the dimensionless parameter

$$\xi_\Omega \equiv \frac{v_\phi}{v_{\text{esc}}} \Big|_{R_*} = \left(\frac{\Omega_*^2 R_*^3}{2GM_*} \right)^{1/2}, \quad (19)$$

and the sound speed is specified by the dimensionless parameter

$$\xi_T \equiv \frac{c_T}{v_{\text{esc}}} \Big|_{R_*} = \left(\frac{c_T^2 R_*}{2GM} \right)^{1/2}. \quad (20)$$

By using these dimensionless parameters, and by using our dimensionless ‘‘code units’’ (Equations 9-11), we can more readily scale the problem to a number of other contexts. This is discussed in more detail in Appendix C.

2.3 Boundary Conditions

At the inner boundary, we enforce boundary conditions such that $\frac{\partial v}{\partial r} = 0$, $\frac{\partial \mathbf{B}'}{\partial r} = 0$, and $v_r \geq 0$ in the ghost zones. We also set the density to preserve (non-rotating) hydrostatic equilibrium across the ghost zones:

$$\rho(r) = \rho_* \exp \left[\frac{1}{2\xi_T^2} \left(\frac{R_*}{r} - 1 \right) \right]. \quad (21)$$

In order to enforce

$$\frac{\partial B'_r}{\partial t'} = 0 \quad (22)$$

at the inner boundary (and thus prevent unchecked growth in \mathbf{B}'), we fix the components of the electric field \mathbf{E}' at the inner boundary:

$$E'_\theta = 0 \quad (23)$$

$$E'_\phi = 0. \quad (24)$$

At the outer boundary, we enforce ‘‘outflow’’ boundary conditions such that:

$$\rho^{N_1+i} = \left(\frac{r^{N_1}}{r^{N_1+i}} \right)^2 \rho^{N_1} \quad (25)$$

$$v_r^{N_1+i} = v_r^{N_1} \quad (26)$$

$$v_\theta^{N_1+i} = \frac{r^{N_1+i}}{r^{N_1}} v_\theta^{N_1} \quad (27)$$

$$(v'_\phi)^{N_1+i} = \frac{r^{N_1+i}}{r^{N_1}} (v'_\phi)^{N_1} \quad (28)$$

$$\mathbf{B}^{N_1+i} = \mathbf{B}^{N_1}, \quad (29)$$

where N_1 is the index of the last active radial zone. The boundary conditions are discussed in greater detail in Appendix D.

2.4 Resolution and Grid

The resolution and box size we use varies depending on the simulation. By convention, we use a $1024 \times 1 \times 1$ grid in 1D (spherical symmetry), a $512 \times 512 \times 1$ grid in 2D (axisymmetry), and a $512 \times 64 \times 128$ grid in full 3D, with a box that has physical extent $r \in [1, 50]R_*$, $\theta \in [0, \pi]$, $\phi \in [0, 2\pi]$ (except in 1D, where the angular extent of the box is reduced to $\theta \in \left[\frac{\pi}{2} - \frac{1}{2}, \frac{\pi}{2} + \frac{1}{2} \right]$, $\phi \in [-0.5, 0.5]$). Zones in the θ and ϕ directions are linearly spaced, while zones in the radial direction are logarithmically spaced.

Some simulations require a larger outer boundary to fully capture the sonic surfaces (see §3.3). For these simulations, we expand the outer boundary to $100R_*$. The number of radial zones used in these simulations is not altered, as, due to the logarithmic spacing in the radial direction, this increase in box size does not lead to a significant reduction in resolution.

2.5 Simulation Stop Time

All of our simulations are evolved until a steady-state behavior emerges. For our 2D simulations, we simulate until $t = 1000$ in our code units (Equations 9) - (11)). However, this is well in excess of the time required for steady state behavior to emerge. For our 3D simulations, we end the simulations early. The time varies between simulations but is in general $t \gtrsim 200$, again in our code units.

3 RESULTS

3.1 Non-Rotating, Non-Magnetic Baseline

We performed high resolution simulations of 1D, non-rotating, non-magnetic (NRNM) Parker winds to serve as a baseline comparison for the rotating and magnetic simulations. In Figure 1, we plot the normalized mass loss rate as a function of the isothermal sound speed. We find that the mass loss rapidly decreases as c_T decreases, falling by several orders of magnitude over a ~ 30 per-cent decrease in c_T . Analytically (Lamers & Cassinelli 1999), the mass loss rate is

$$\dot{M} = \frac{\pi}{4} R_*^2 \rho_* c_T \left(\frac{v_{\text{esc}}}{c_T} \right)^4 \exp \left[\frac{3}{2} - \frac{v_{\text{esc}}^2}{2c_T^2} \right], \quad (30)$$

where v_{esc} is the escape velocity at $r = R_*$. We see that our simulations closely follow the analytic solution (to within a few percent at this resolution; see §2.4 and §3.5 for more details regarding convergence).

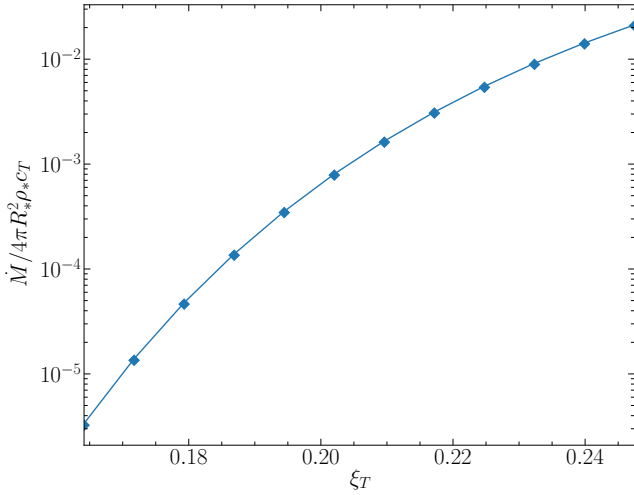


Figure 1. Normalized mass loss rate versus the isothermal sound speed (blue points), and the analytic solution (Equation 30) for a pure isothermal wind (orange curve).

3.2 Properties of the Magnetized Winds

In Figure 2, we present the results of a suite of 2D axisymmetric simulations across a parameter space of $0.1414 \leq \xi_T \leq 0.2475$ and $0.0174 \leq \xi_\Omega \leq 0.2777$, for $\xi_B = 4.63 \times 10^{-2}$. The data summarized in this figure is also presented in table form in Appendix E. We discuss each panel of this figure in the following sections.

In certain cases with low ξ_T and high ξ_Ω (the bottom left portion of the panels in Figure 2), we encounter significant numerical errors that prevent us from completing accurate simulations using those parameters. This region is colored in white in the figure and is not included in Appendix E.

3.2.1 Mass Loss Rate

In the steady-state limit, the continuity equation (Equation 1) implies that²

$$\dot{M} = \oint r^2 \rho v_r d\Omega = \text{constant}. \quad (31)$$

Unlike in the spherically symmetric case, however, the mass flux is not equally distributed over solid angle; i.e., $\dot{M} \neq 4\pi r^2 \rho v_r$. We plot the mass loss rate (normalized to PNS values) in panel (a) of Figure 2. As in the NRNM case, we find that the mass loss rate is a strong function of the sound speed, but in addition, that there is a substantial centrifugal enhancement to \dot{M} for large ξ_Ω , as can be seen by the downturn of the \dot{M} contours.

Specifically, the \dot{M} values shown in Figure 2 are the mass-weighted radial averages, i.e.,

$$\langle \dot{M} \rangle = \frac{\sum_r \dot{M} M_r}{\sum_r M_r} \quad (32)$$

where M_r is the sum of cell masses over the spherical surface at radial coordinate r :

$$M_r = \sum_{\theta, \phi} \rho r^2 \sin \theta \Delta_r \Delta_\theta \Delta_\phi, \quad (33)$$

² $d\Omega$ here is the solid angle element, $d\Omega = \sin \theta d\theta d\phi$, and should not be confused with the angular speed Ω .

where \sum_k indicates the sum over all cells in the k -direction, and Δ_k is the cell width in the k -direction. The sum is taken over all cells with $r > 10R_*$ (except the outer 5 cells, which are excluded to ignore boundary effects). We use a similar method to measure the other quantities shown in Figure 2, but in the case of Φ_{open} (see below), the average is taken for all $r > 30R_*$ to ensure that the average only includes open field lines.

3.2.2 Angular Momentum Loss Rate

Following the derivation in Vidotto et al. (2014), the z -component of the angular momentum flux across a closed spherical surface is given by,

$$j = \oint r^2 \rho v_r \varpi \left(v_\phi - \frac{B_r B_\phi}{4\pi \rho v_r} \right) d\Omega, \quad (34)$$

where $\varpi = r \sin \theta$ is the cylindrical radius. Because the angular momentum of the magnetar is aligned with the z -axis (in both the aligned and tilted cases), this is the only relevant component of the flux. We plot this quantity in panel (b) of Figure 2.

We can also use the angular momentum loss rate to define the spindown timescale:

$$\tau_J = \frac{J}{\dot{J}}, \quad (35)$$

where J is the angular momentum of the star, which we take to be that of a uniform density spherical star,

$$J = \frac{2}{5} M R_*^2 \Omega_*. \quad (36)$$

The spindown timescale is shown in panel (e) of Figure 2.

3.2.3 Energy Loss Rate

For an equatorial rotator (i.e., one with $v_\theta = B_\theta = 0$; e.g., Weber & Davis 1967)³, one can show that the quantity

$$\mathcal{B}_{\text{eq}} \equiv \frac{1}{2} (v_r^2 + v_\theta^2 + v_\phi^2) + c_T^2 \log \frac{\rho}{\rho_*} - \frac{GM}{r} - \frac{\varpi \Omega_* B_r B_\phi}{4\pi \rho v_r} \quad (37)$$

is conserved, i.e., $\partial \mathcal{B}_{\text{eq}} / \partial r = 0$ (Lamers & Cassinelli 1999). The first term in this quantity is the kinetic energy flux, the second is the thermal energy flux, the third is gravitational, and the fourth is magnetic. We note that the thermal term is negative (because ρ decreases with radius) and the fourth is positive (because $B_\phi < 0$).

We generalize this conservation law to the non-equatorial case by defining the (conserved) energy flux across a closed spherical surface to be:

$$\dot{E} = \oint r^2 \rho v_r \mathcal{B}_{\text{eq}} d\Omega. \quad (38)$$

Formally, \dot{E} is only constant for an equatorial rotator, however, we find that the deviation from constant \dot{E} is small. We plot the energy loss rate in panel (c) of Figure 2.

Analytically (e.g., Metzger et al. 2007), we expect the energy loss rate in the fast magnetic rotator (FMR) regime (where magnetocentrifugal forces dominate; Lamers & Cassinelli 1999) to scale as

$$\dot{E}_{\text{FMR}} \sim \frac{3}{2} \dot{M} \eta v_M^2, \quad (39)$$

³ Though we explicitly include the v_θ term in our calculations.

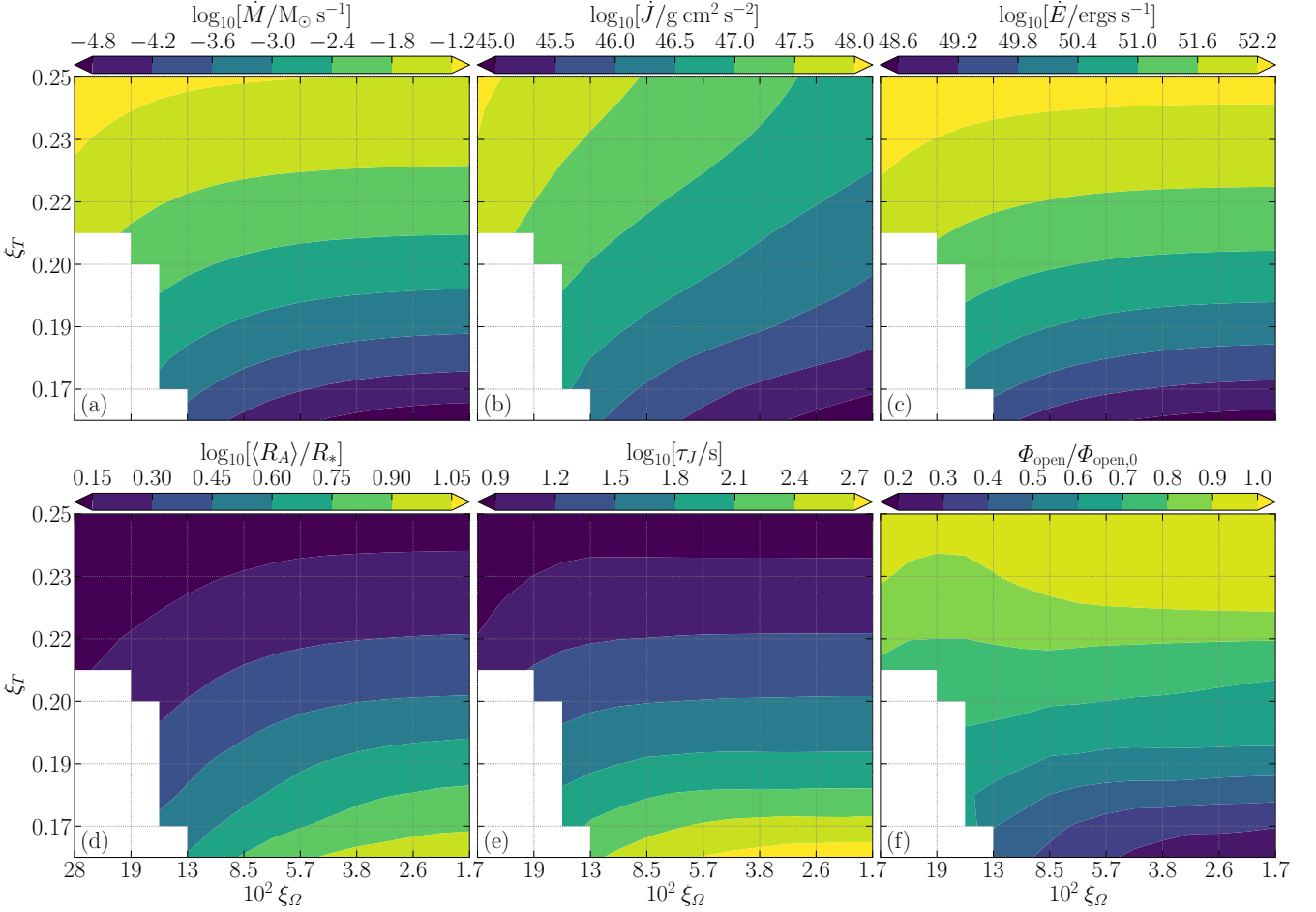


Figure 2. From left to right, top to bottom: (a) the wind mass loss rate, (b) angular momentum loss rate (i.e., wind torque), (c) energy loss rate, (d) average Alfvén radius, (e) spindown time, and (f) unsigned open magnetic flux, over a grid in dimensionless isothermal sound speed ξ_T (Equation 20) and dimensionless rotation rate ξ_Ω (Equation 19), for a magnetic field of $\xi_B = 4.63 \times 10^{-2}$. For dimensional quantities (panels a, b, c, e), the units assume parameters are scaled to the proto-magnetar regime (see §4 and Appendix C for more details). With the exception of \dot{J} , which remains a strong function of ξ_Ω even at small rotation rates, these quantities are all strong functions of ξ_T and weak functions of ξ_Ω except for the most rapid rotators.

where $\eta = \Omega \dot{J} / \dot{E}$ is the ratio of spindown power to asymptotic wind power, and

$$v_M = \left(\frac{\Phi_{\text{open}}^2 \Omega_*^2}{\dot{M} c^3} \right)^{1/3} \quad c = \sigma^{1/3} c \quad (40)$$

is the Michel velocity (Michel 1969), σ is the wind magnetization (Lamers & Cassinelli 1999; Metzger et al. 2007), and Φ_{open} is the open magnetic field flux (defined below). For most FMR cases, $\eta \approx 1$, but for FMRs with small B_* and short periods, most of the spindown power is used to unbind the wind, and thus $\eta \gg 1$ (Metzger et al. 2011). For thermally driven cases (where magnetocentrifugal forces are negligible), $\eta \ll 1$, because the spindown power does not make an appreciable contribution to the asymptotic wind power. Because our parameter space spans the regime from thermally driven winds to FMRs, this thermal component makes a large contribution to the total asymptotic wind power in many of our simulations. We find that the addition of an additional thermal term,

$$\dot{E}_{\text{th}} \approx \dot{M} c_T^2, \quad (41)$$

provides a more accurate estimate to our measured energy fluxes.

The wind magnetization σ is also a measure of how relativistic the wind, as $\sigma \sim S$, where S is the Poynting flux. We typically say the wind is relativistic when $\sigma > 1$. We do find that a small number of our simulations (those with the smallest ξ_T and largest ξ_Ω) have $\sigma > 1$, however, the effects of relativity on these winds is outside the scope of this paper.

3.2.4 Alfvén Radius

In a 1D magnetized wind, the Alfvén point is the point where the wind velocity is equal to the Alfvén velocity, given by

$$v_A = \frac{B^2}{4\pi\rho}. \quad (42)$$

In higher dimensions, we define an Alfvén surface \mathcal{S}_A that is the locus of all points where $v_p = v_A$, where

$$v_p^2 = v_r^2 + v_\theta^2 \quad (43)$$

is the poloidal velocity. We also define B using the poloidal field strength B_p , defined analogously to the poloidal velocity. In principle, we could numerically solve for \mathcal{S}_A in our simulation data and then use that to compute an average Alfvén radius $\langle R_A \rangle$. However,

it is far more convenient to determine $\langle R_A \rangle$ from the eigenvalues of the problem i.e., \dot{M} and \dot{J} . Consider that the angular momentum loss rate can also be written as

$$\dot{J} = \dot{M} R_A^2 \Omega_*. \quad (44)$$

Since we have already computed \dot{M} and \dot{J} in the previous sections, it is straightforward to use them to compute an average Alfvén radius,

$$\langle R_A \rangle = \sqrt{\frac{\dot{J}}{\dot{M} \Omega_*}}. \quad (45)$$

We plot this quantity in panel (d) of Figure 2.

3.2.5 Open Magnetic Field Flux

The unsigned open magnetic field flux is given by:

$$\Phi_{\text{open}} = \oint r^2 |B_r| d\Omega. \quad (46)$$

At large radii, this quantity is constant, because all field lines are open. However, close to the surface, a region of closed magnetic field lines can develop, reducing Φ_{open} . The ratio of Φ_{open} at these two locations, then, provides a measure of the shape of the magnetic field. As $\Phi_{\text{open}}/\Phi_{\text{open},0}$ increases, the surface magnetic field becomes more and more open, with $\Phi_{\text{open}}/\Phi_{\text{open},0} = 1$ corresponding to a split-monopole field. We plot this ratio in panel (f) of Figure 2.

3.3 Structure and Evolution of the Magnetized Winds

Here, we examine a selection of our 2D simulations in more detail. In Figures 3 and 4, we show the poloidal mach number v_p/c_T and plasma β , defined as the ratio of thermal pressure to magnetic pressure:

$$\beta = \frac{2c_T^2 \rho}{B^2}, \quad (47)$$

in the final snapshots of our simulations. We plot the inner $20R_* \times 20R_*$ (40 percent of the total radial extent) region for each model in each of these figures, which is enough to capture the sonic surfaces (see below) at the equator in all cases, though the sonic surfaces at the poles is sometimes outside this region. We also present a zoomed in ($10R_* \times 10R_*$) panel of a single one of the simulations in Figure 5, to better show the structure of the magnetic field near the surface of the star.

We define four *sonic surfaces* in these plots. On the Mach surface \mathcal{S}_M , the poloidal speed of the wind v_p is equal to the isothermal sound speed c_T . On the Alfvén surface \mathcal{S}_A , the poloidal speed is equal to the Alfvén speed v_A . On the fast and slow magnetosonic surfaces \mathcal{S}_\pm , the poloidal speed is equal to the fast or slow magnetosonic speed:

$$v_p^2 = v_\pm^2 \equiv \frac{1}{2} \left(v_A^2 + c_T^2 \pm \sqrt{(v_A^2 + c_T^2)^2 - 4v_A^2 c_T^2 \cos^2 \vartheta} \right), \quad (48)$$

where ϑ is the angle between the magnetic field and the direction of wave propagation. For the purposes of determining \mathcal{S}_\pm , we assume that magnetosonic waves propagate radially, i.e.,

$$\cos \vartheta = \frac{\mathbf{B} \cdot \hat{\mathbf{f}}}{B}. \quad (49)$$

The magnetic forces are more dynamically important at low sound speeds than they are at higher sound speeds, where thermal effects dominate. Thus, at lower ξ_T , the sonic surfaces $\mathcal{S}_A, \mathcal{S}_\pm$ move outwards. The Mach surface \mathcal{S}_M also naturally moves outward at lower

sound speed as $r_s \sim c_T^{-2}$. At larger ξ_Q , the rotational velocity, which decreases with the *cylindrical* radius ϖ , becomes more dynamically important. Thus, the sonic surfaces take on a more cylindrical quality, moving further out at the poles than at the equator (Keppens & Goedbloed 2000).

In Figure 6, we plot the density and Mach number profiles of a subset of our simulations, where the Mach number is defined as

$$\mathcal{M} = \frac{v}{c_T}, \quad (50)$$

for some characteristic velocity v (e.g., $\mathcal{M}_p = v_p/c_T$ is the poloidal Mach number and $\mathcal{M}_A = v_A/c_T$ is the Alfvénic Mach number). In each set of panels, each column corresponds to the simulations shown in Figures 3 and 4, respectively. We see the density profile is highly dependent on both the sound speed and the rotation rate, with cooler (i.e., lower ξ_T) models seeing a relatively larger effect from rotation. Hot models also have larger outflow velocities than cooler models do. Rapid rotation also changes the shape of the Mach number profile – as the rate of rotation increases, \mathcal{M}_p increases at small radii, but remains relatively constant at large radii.

3.4 Effect of Magnetosphere Tilt

We simulated a smaller number of 3D models with tilt angles $\alpha > 0$, at representative regions of parameter space. Snapshots of some of these simulations are presented in Figure 7. We note that the $\alpha = 0$ case is not identical to the 2D simulation of the same ξ_T and ξ_Q . There is a small asymmetry in the current sheet, which, in our 2D simulations lies exactly along the equator. The degree of asymmetry increases for cooler and more rapidly rotating (smaller ξ_T and larger ξ_Q) simulations, and leads to significant uncertainties in \dot{M} , \dot{J} , and \dot{E} .

In Figure 8, we investigate how \dot{M} , \dot{J} , \dot{E} , and Φ_{open} are affected by the tilt, in simulations with 4 different combinations of ξ_T and ξ_Q . We find that \dot{M} , and \dot{E} are very nearly constant with tilt angle (at most, varying by ~ 1 per-cent over the full range of α). By contrast, \dot{J} and Φ_{open} show strong trends with α . This implies that the trends in these quantities are driven by intrinsic effects of the misaligned magnetic field, rather than as a consequence of a trend in the mass loss rate. However, these trends break down in our low ξ_T simulations, shown in the lower two panels of the figure.

In the simplest model of the magnetic field, where the field lines are purely radial, we would expect Φ_{open} to remain constant with α , as the magnetic field strength is independent of angle. For higher order moments, the polar field strength is twice the equatorial field strength, and Φ_{open} starts to vary with α as different parts of the magnetosphere are opened by the wind and by centrifugal forces. For the aligned ($\alpha = 0$) case, the open field lines are located near the poles, where $\dot{J} = 0$. As the tilt angle increases, more open field lines are equatorial, and \dot{J} along open field lines increases. As mass is ejected only along open field lines, we would then expect that larger tilt angles would mean larger \dot{J} . As for \dot{E} , we would expect that for more thermally dominated simulations, such as the ones shown in Figure 8, the trends in \dot{E} will closely follow the trends in \dot{M} (as $\dot{E} \sim \dot{M} c_T^2$ in thermally dominated winds). In the FMR regime, we would expect the trend on \dot{E} to track the trends in Φ_{open} . However, a full study of how these quantities vary over the complete three-dimensional parameter space of (ξ_T, ξ_Q, α) is beyond the scope of this paper.

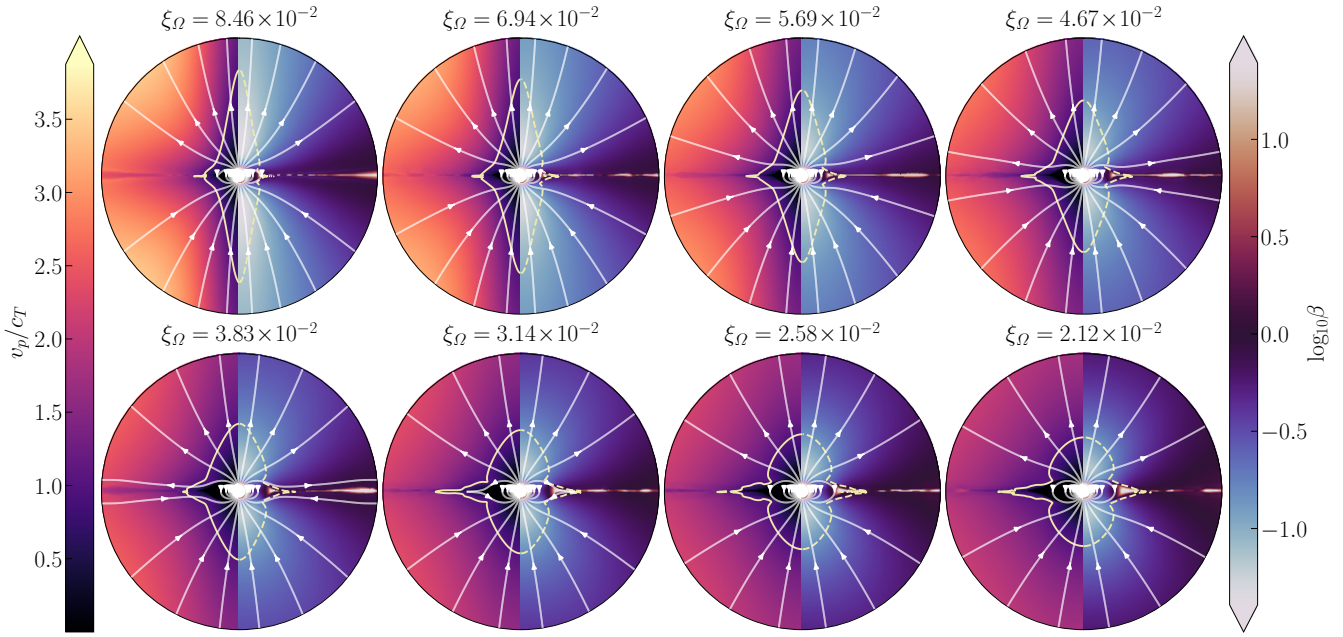


Figure 3. The inner $20R_*$ of 2D axisymmetric simulations at various rotation periods for a fixed sound speed $\xi_T = 0.1641$. On the left hand side the poloidal mach number $\mathcal{M} = v_p/c_T$ is shown; on the right hand side the plasma β is shown. The contours in yellow show the sonic surfaces: the mach surface \mathcal{S}_M on the LHS, and the slow magnetosonic surface \mathcal{S}_- (dashed) on the RHS. The magnetic field lines are shown in white on both sides. As the rotation period is lowered, the centrifugal forces become larger and the sonic surfaces become more cylindrical. At the same time, the region of closed magnetic field lines becomes bigger.

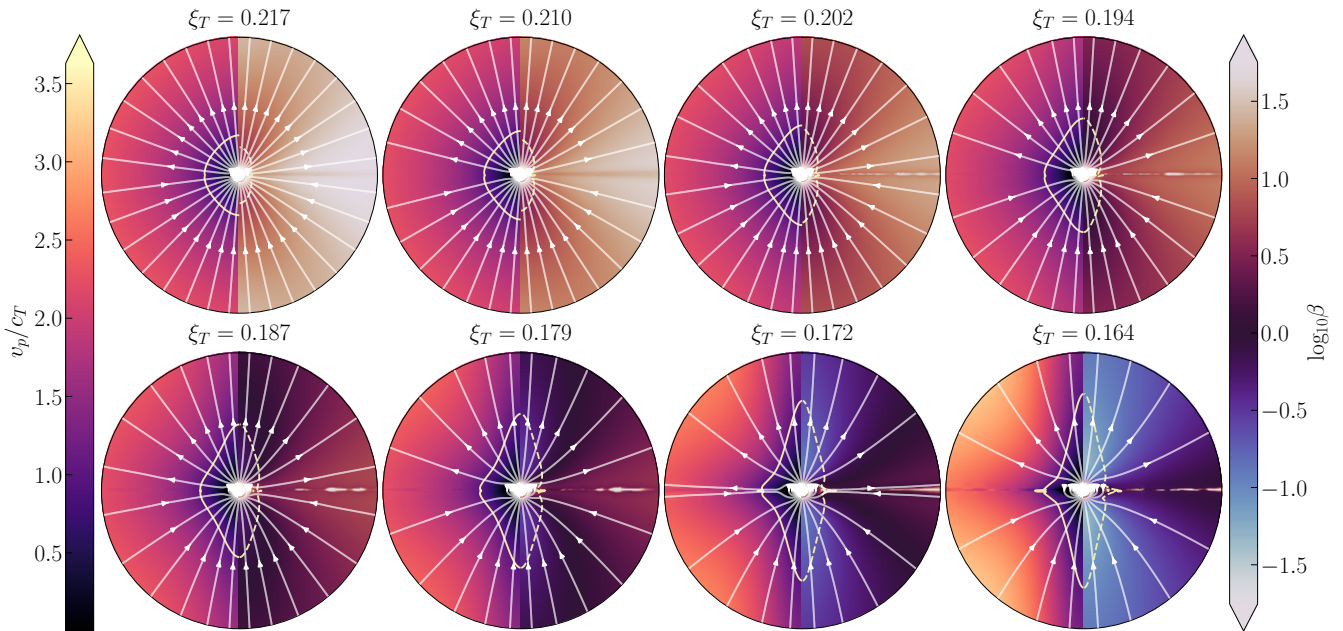


Figure 4. The same as Figure 3, but for varying sound speed at a fixed, moderate rotation rate $\xi_\Omega = 6.94 \times 10^{-2}$. As the sound speed is lowered, the simulation becomes more magnetically dominated and sonic surfaces move to larger radii. The mach surface becomes more oblate, and a pronounced cusp appears in all surfaces on the equator. Furthermore, we note that as the sound speed decreases, the wind is more and more directed into two off-equatorial lobes, and a region of closed magnetic field lines forms in the subsonic region around the equator.

3.5 Resolution Effects

In Figure 9, we examine the effects of radial resolution on our measurement of \dot{M} and the sonic radius r_s in our NRNM simulations, for 1D and 2D simulations. We find that our measurements of the sonic radius converge more quickly with increasing radial resolution

than our measurements of the mass loss rate. Furthermore, the move

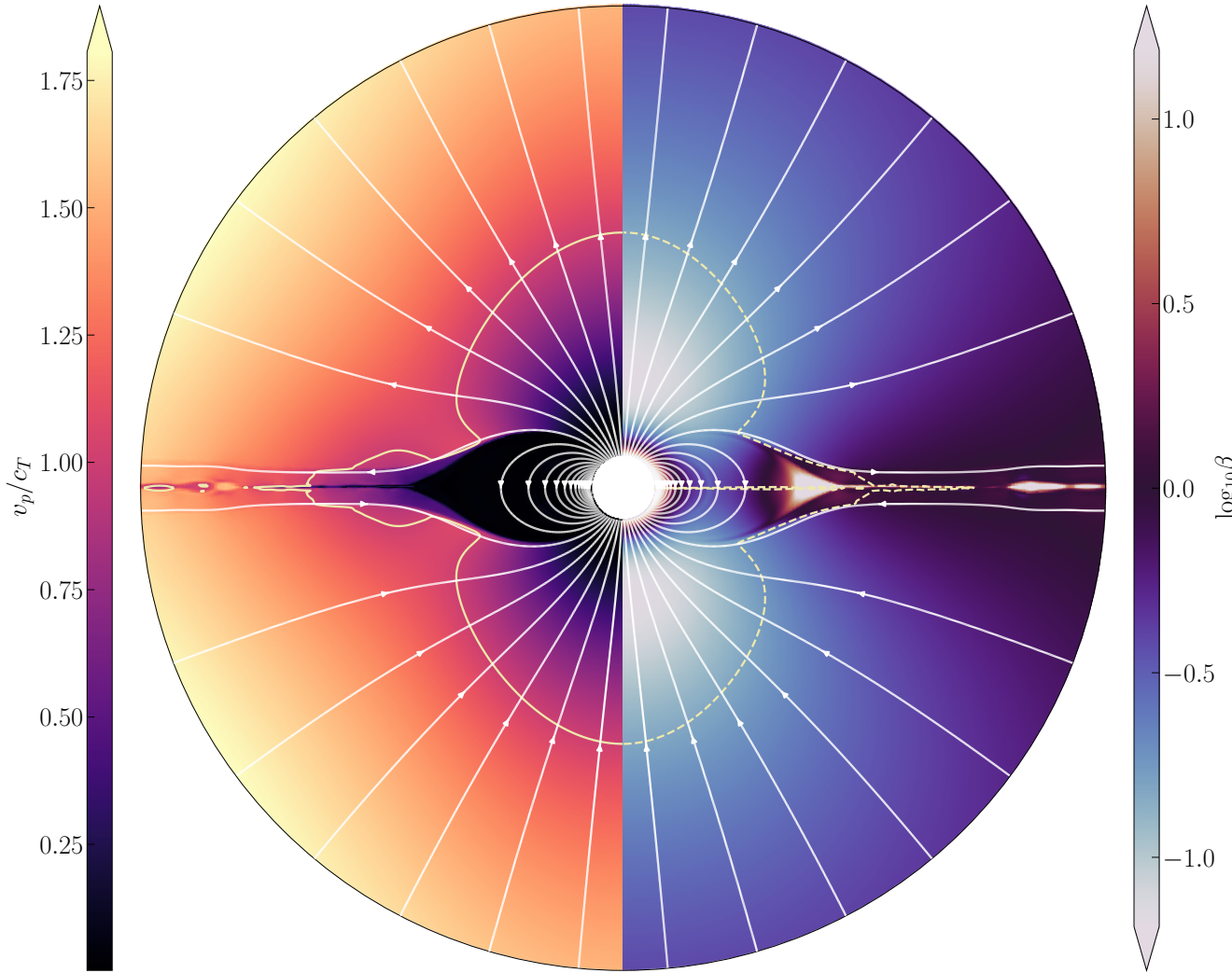


Figure 5. Zoom-in to the inner $15R_*$ of the 2D simulation with $\xi_T = 0.1641$ and $\xi_\Omega = 2.12 \times 10^{-2}$. From this plot, it is clear that the poloidal velocity of the wind in the closed zone is zero (or nearly zero). Furthermore, as the closed field lines come to a cusp at the edge of the closed zone, the plasma β increases sharply.

from one to two spatial dimensions does not significantly affect the rate of convergence⁴.

In Figure 10, we examine the convergence of 2D simulations with $\xi_T = 0.1641$, $\xi_\Omega = 2.12 \times 10^{-2}$, and $\xi_B = 4.63 \times 10^{-2}$ (the same parameters as the simulation shown in Figure 5). We find that the wind properties \dot{M} , \dot{J} , and \dot{E} readily converge with increasing radial resolution, but stay relatively constant with increasing angular resolution, consistent with the NRNM expectations. This result is consistent for both high and low ξ_T and ξ_Ω . This helps justify our use of relatively lower angular resolution in our 3D models.

4 DISCUSSION

The results shown in the previous section can be scaled to a number of physical systems of interest, by using different values of ρ_* , GM_* ,

⁴ However, in 2D, and especially in 3D, we are forced to run at lower resolution in order to maintain reasonable simulation walltimes, which limits the resolution that is practically available to us.

and R_* when converting from code units to physical units. This is discussed in more detail in Appendix C. Because the field strength and rotation rate are specified with the dimensionless parameters ξ_B (Equation 18) and ξ_Ω (Equation 19), they also naturally scale with our choice of units (though not necessarily to values appropriate for the regime of interest). We summarize the scalings we use in Table 1.

Below, we focus on the application to newly-born highly-magnetic and rapidly-rotating proto-neutron stars, and then discuss other applications of our results.

4.1 Analytic Approximations

For the purpose of analytical estimation, we closely follow the analysis of Thompson et al. (2003). Consider a star with a simplified magnetic field structure with

$$B_p = B_* \left(\frac{R_*}{r} \right)^\lambda, \quad (51)$$

For a split monopole field structure, (e.g., Weber & Davis 1967), $\lambda = 2$, and for a dipole field, $\lambda = 3$. Therefore, we should expect that

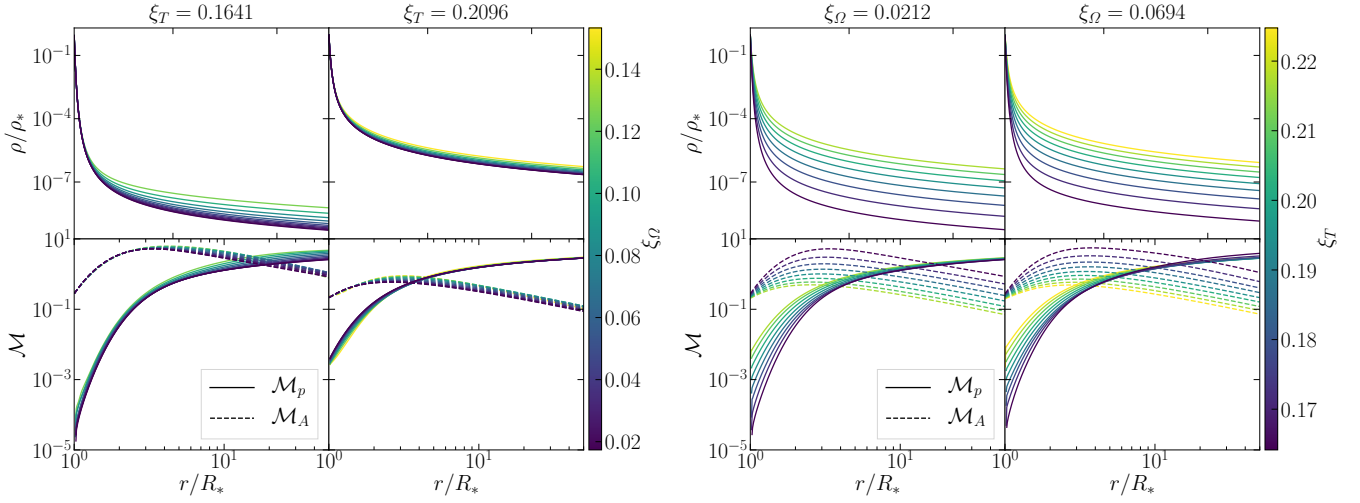


Figure 6. Density and mach number ($M = v/c_T$) profiles for simulations at varying ξ_T and ξ_Ω . The left two panels show constant ξ_T and varying ξ_Ω , while the right two panel show the reverse. Profiles are taken at $\theta = \pi/8$. For cooler models, rotation has a larger impact on the structure of the wind. In particular, more rapidly rotating models have larger ρ and M_p , with both effects diminishing at larger ξ_T .

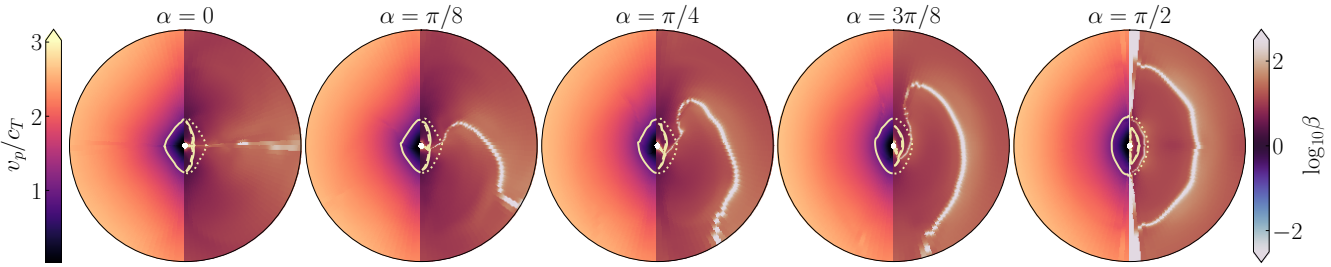


Figure 7. The inner $30R_*$ of the $\phi' = 0$ slice of 3D simulations with varying magnetosphere tilt α at fixed rotation rate $\xi_\Omega = 0.085$ and sound speed $\xi_T = 0.210$. Contours depict the sonic surfaces as described in Figure 3, with the addition of the Alfvén surface (solid) and fast magnetosonic surface (dotted). We note that even in the aligned ($\alpha = 0$) simulation, a small tilt develops due to spontaneous symmetry breaking. The magnitude of this effect, and the resultant deviation from 2D simulations, is greater for cooler and more rapidly rotating simulations (see Figure 8); for the simulation in question it leads to a ~ 0.5 per-cent deviation in \dot{M} and \dot{E} and a ~ 10 per-cent deviation in \dot{J} and Φ .

Quantity	Code Units	Proto-Magnetar	Sun-like Star ^a	Hot Jupiter ^b
ρ_*	1	$10^{11} \text{ g cm}^{-3}$	$10^{-16} \text{ g cm}^{-3}$	$10^{-15} \text{ g cm}^{-3}$
M_*^c	$1/G$	$1.4 M_\odot$	$1 M_\odot$	$0.7 M_J$
R_*	1	10 km	$1 R_\odot$	$1.4 R_J$
B_*	0.0655	10^{15} G	0.101 G	0.0221 G
P_*	16 to 256	1.2 to 19 ms	0.29 to 4.7 d	14.5 to 231 h
c_T	0.2 to 0.35	0.091 to 0.16 c	87 to 150 km s^{-1}	6.02 to 10.5 km s^{-1}

Table 1. Summary of the scaling factors to the various contexts considered here. In addition to ρ_* , GM , and R , which together define the unit conversion, we also show the range of values for B_* , P_* , and c_T , as determined by the ξ_B , ξ_Ω , and ξ_T ranges given in §3.2. Since the ranges of these values were deliberately chosen to cover the proto-magnetar regime, they do not always produce appropriate values in other contexts.

^a ρ_* in this case is chosen such that $\dot{M} \sim \dot{M}_\odot \approx 2 \times 10^{12} \text{ g s}^{-1}$ for a ξ_B and ξ_Ω similar to that used in Finley & Matt (2017). See §4.3.1 for details.

^b Using the Murray-Clay et al. (2009) values for ρ_* , M_* , and R_* .

^c The quantity GM_* is specified in the code; M_* is presented here on its own for the sake of readability.

some $2 < \lambda < 3$ to best describe the magnetic field structure of our simulations, depending on the sound speed c_T . From this equation, we find that

$$R_A^{2\lambda-2} = B_*^2 R_*^{2\lambda} \dot{M}^{-1} v_A^{-1}, \quad (52)$$

assuming spherical outflow (i.e., $\dot{M} = 4\pi\rho v_r$ and $v_p = v_r$).

As discussed in Lamers & Cassinelli (1999); Thompson et al. (2004); Metzger et al. (2007), basic scalings for magnetocentrifugal

spindown is provided by assuming effective co-rotation of the wind material out to the Alfvén point, where

$$R_A^2 \Omega_*^2 = \frac{3}{2} \eta v_M^2 = \frac{3}{2} \eta \left(\frac{R_*^4 B_*^2 \Omega_*^2}{\dot{M}} \right)^2, \quad (53)$$

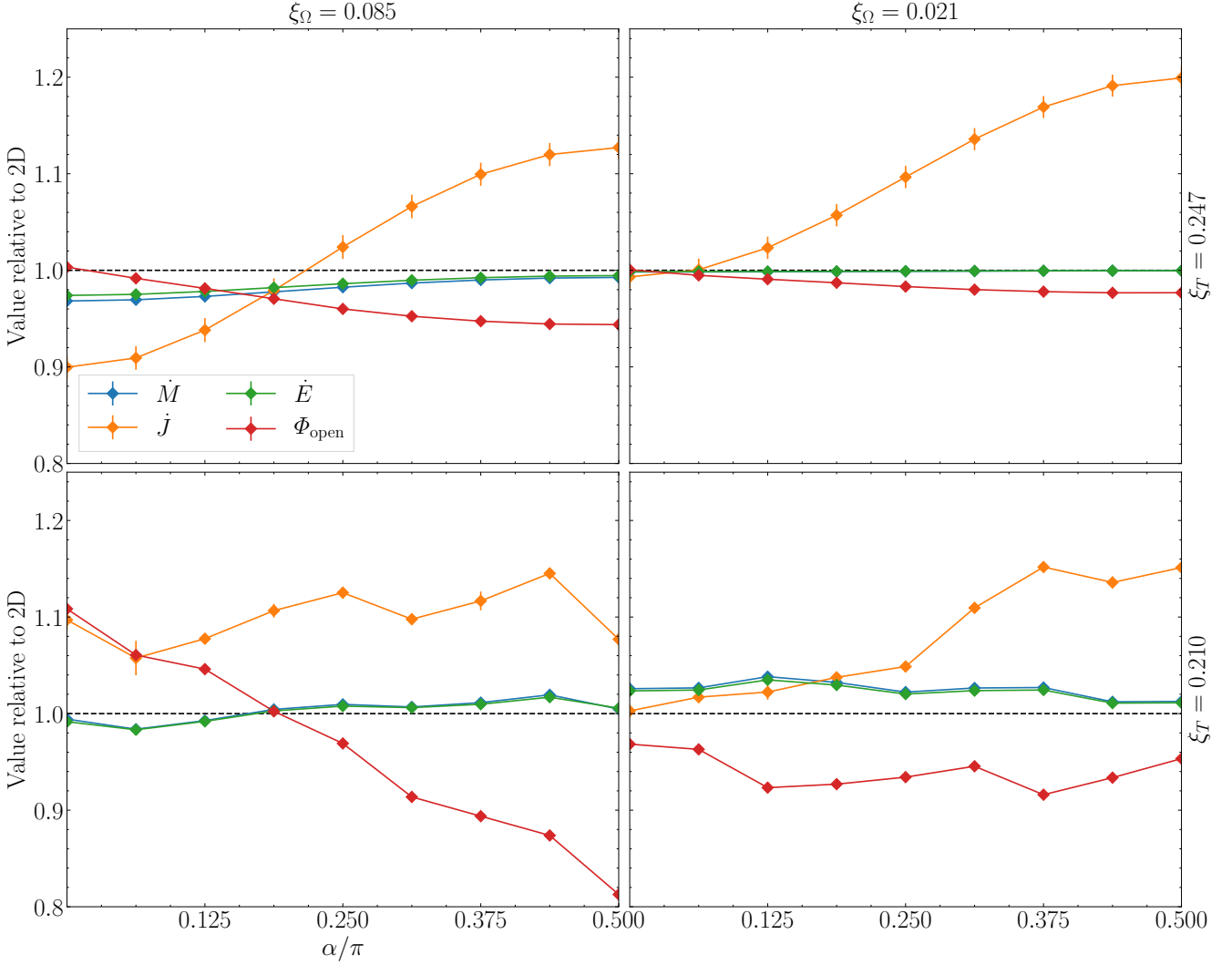


Figure 8. \dot{M} , \dot{J} , \dot{E} , and Φ_{open} (normalized by their value in the aligned case) as a function of the tilt angle α for a series of 3D simulations at different ξ_T and ξ_Ω . We identify broad trends in these results – \dot{J} tends to decrease as α increases, while Φ decreases. \dot{M} and \dot{J} , on the other hand, stay relatively constant. These trends break down in cooler and more rapidly rotating simulations.

For a spherical wind, the Alfvén speed can thus be estimated as

$$v_A = \frac{v_M^3}{R_A^2 \Omega_*^2} = \left(\frac{2}{3\eta}\right)^{3/2} R_A \Omega_*. \quad (54)$$

This can be incorporated into our estimate for the Alfvén radius,

$$R_A^{2\lambda-1} = \left(\frac{3\eta}{2}\right)^{3/2} B_*^2 R_*^{2\lambda} \dot{M}^{-1} \Omega_*^{-1} \quad (55)$$

We can use this framework to estimate the angular momentum loss rate, and thus, the spindown time. Starting with Equation (34), and assuming that $v_\phi = R_A \Omega_*$ and $B_\phi/B_r|_{S_A} \ll 1$, we find

$$\dot{J} \approx \frac{\pi}{4} \dot{M} R_A^2 \Omega_*. \quad (56)$$

Once again assuming the star is a uniform density sphere, we find the spindown time to be

$$\tau_J = \frac{8}{5\pi} M_* \left[\dot{M}^{3-2\lambda} B_*^{-4} R_*^{-2} \Omega_*^2 \left(\frac{3\eta}{2}\right)^{-3} \right]^{1/(2\lambda-1)}. \quad (57)$$

Scaling these to values appropriate to the proto-magnetar regime (see Table 1), we find

$$\tau_J \approx \begin{cases} 30\eta^{-1} B_{*,15}^{-4/3} \dot{M}_{-3}^{-1/3} P_{*,6}^{-2/3} R_{*,6}^{-2/3} \text{ s} & \lambda = 2 \\ 100\eta^{-3/5} B_{*,15}^{-4/5} \dot{M}_{-3}^{-3/5} P_{*,6}^{-2/5} R_{*,6}^{-2/5} \text{ s} & \lambda = 3 \end{cases}, \quad (58)$$

where $B_{*,x} = B_*/10^x \text{ G}$, $\dot{M}_x = \dot{M}/10^x M_\odot \text{ s}^{-1}$, $P_{*,x} = P_*/10^x \text{ s}$, and $R_{*,x} = R_*/10^x \text{ cm}$. For sun-like stars, we would expect (for $\lambda = 3$)

$$\tau_J \approx 2 \times 10^{18} \eta^{-3/5} B_{*,1}^{-4/5} \dot{M}_{-21}^{-3/5} P_{*,6}^{-2/5} R_{*,\odot}^{-2/5} \text{ s}, \quad (59)$$

and for Hot Jupiters (also for $\lambda = 3$),

$$\tau_J \approx 3 \times 10^{17} \eta^{-3/5} B_{*,0}^{-4/5} \dot{M}_{-22}^{-3/5} P_{*,5}^{-2/5} R_{*,J}^{-2/5} \text{ s}, \quad (60)$$

where $R_{*,\odot} = R_*/1 R_\odot$ and $R_{*,J} = R_*/1 R_J$.

This analysis only applies when the asymptotic velocity is dominated by the rotation. For slow rotators, the Alfvén velocity

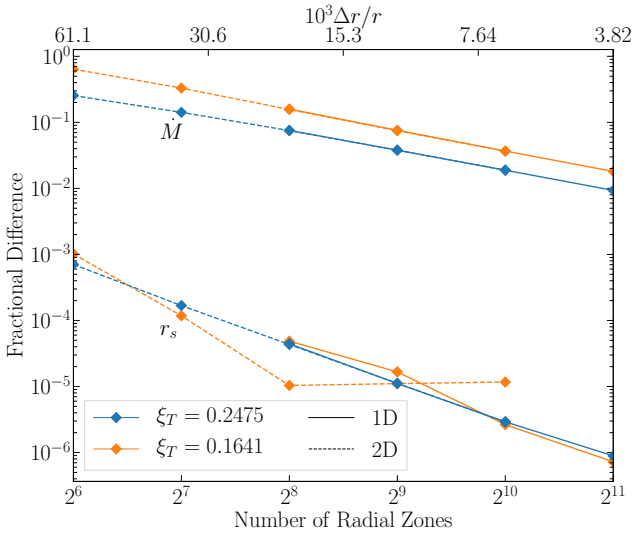


Figure 9. Fractional difference in \dot{M} and r_s (compared to the analytic values as given by Equations (14) and (30)) vs the number of radial zones (or, equivalently, the fractional spacing $\Delta r/r$, shown at top), for “high” ($\xi_T = 0.2475$) and “low” ($\xi_T = 0.1641$) isothermal sound speeds, for the 1D (solid) and 2D (dashed) NRNM simulations. The mass accretion rate converges much more slowly than the sonic radius, and to lower accuracy. However, the sound speed does not meaningfully affect the rate of convergence.

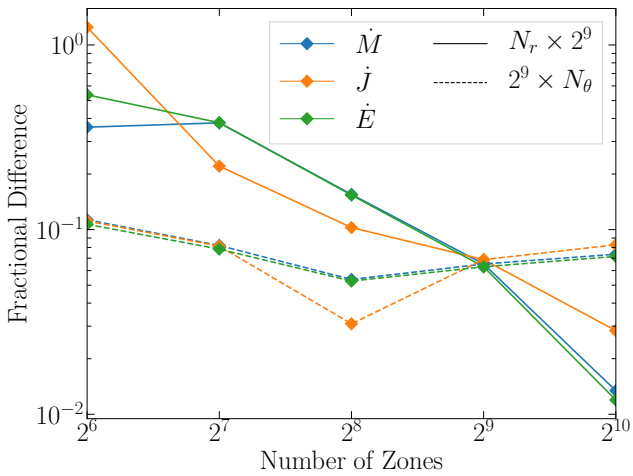


Figure 10. Fractional difference in \dot{M} , J , and \dot{E} , and r_s vs the number of zones for 2D simulations with $\xi_T = 0.1641$, $\xi_\Omega = 2.12 \times 10^{-2}$, and $\xi_B = 4.63 \times 10^{-2}$. Solid lines show the case of fixed angular resolution (at the fiducial resolution specified in §2.4) and varying radial resolution, while the dashed lines show the case of fixed radial resolution and varying angular resolution. We see that increasing the angular resolution has only a marginal impact on the precision of our measurements; simulating with high radial resolution is of far greater importance in making precise measurements of the wind properties.

will be of order the sound speed.⁵ In this case, the spindown time is nearly independent of rotation rate (as is visually apparent in

⁵ Technically, the velocity should be of the form $v_A^2 \sim R_A^2 \Omega_*^2 + c_T^2$, but the equations are intractable when the velocity is in this form.

Figure 2c).

$$\tau_J \propto \left(\frac{B_* R_*^\lambda}{c_T \dot{M}^\lambda} \right)^{\frac{1}{\lambda-1}}. \quad (61)$$

It should be noted that the mass loss rate is not a constant $\dot{M} = 10^{-3} M_\odot \text{ s}^{-1}$ (in the proto-magnetar case). As can be seen in Figure 2a, it varies by several orders of magnitude across our parameter space, as a strong function of the sound speed and a weaker, but still significant, function of rotation. Following Metzger (2009), we can describe this as

$$\dot{M} \sim \dot{M}_{\text{NRNM}} f_{\text{cen}} f_{\text{open}}, \quad (62)$$

where \dot{M}_{NRNM} is given by Equation 30, and

$$f_{\text{cen}} \sim \exp \left[\frac{R_*^2 \Omega^2}{c_T^2} \right], \quad f_{\text{open}} \sim \frac{\Phi_{\text{open}}}{4\pi R_*^2 B_*}. \quad (63)$$

Furthermore, when comparing to 2D and 3D results, it should be noted that this analysis assumes spherically symmetric outflow, but in a real simulation, density and \dot{M} are a function of θ . Moreover, in 3D, we must contend with question of tilted magnetospheres. Metzger et al. (2011) suggest that the open magnetic field flux Φ_{open} should be corrected by a factor of $\sqrt{1 + \sin^2 \alpha}$, and that $\dot{E} \propto f_{\text{open}}^{4/3}$ in the non-relativistic limit. Because $\dot{E} \sim \Omega J$, we should also have $J \propto (1 + \sin^2 \alpha)^{2/3}$, and thus:

$$\tau_J \propto (1 + \sin^2 \alpha)^{-2/3}. \quad (64)$$

4.2 Application to Proto-Magnetar Winds

Immediately after a successful massive star supernova explosion, the hot proto-neutron star drives a neutrino-heated thermal wind into the surrounding medium as it radiates its gravitational binding energy over a timescale $\tau \sim 10 - 100$ s (Burrows et al. 1995; Janka & Müller 1996). The wind has been studied as a site for heavy element r -process nucleosynthesis (e.g., Qian & Woosley 1996; Otsuki et al. 2000; Thompson et al. 2001; Thompson & ud Doula 2018). For a sufficiently large magnetic fields, the wind will be magnetically-dominated (Thompson 2003; Thompson et al. 2005) and with rapid enough rotation, the spindown power carried in the outflow could energize supernovae and potentially produce GRBs (Thompson et al. 2004; Bucciantini et al. 2006; Metzger 2009; Bucciantini et al. 2009; Metzger et al. 2011). The model is of direct relevance to the interpretation of SLSNe (Kasen & Bildsten 2010; Woosley 2010). Spindown power has also been suggested as a mechanism for normal Type-IIP SNe (Sukhbold & Thompson 2017).

One metric for assessing when the rotational energy can become dynamically important is when it approaches the kinetic energies of observed explosions

$$E_{\text{rot}} \simeq 1 \times 10^{51} \text{ ergs} \left(\frac{M_*}{1.4 M_\odot} \right) \left(\frac{R_*}{12 \text{ km}} \right)^2 \left(\frac{8 \text{ ms}}{P} \right)^2. \quad (65)$$

From fitting numerical models to GRB data and to the observed lightcurves of SLSNe one finds broadly that GRBs require equivalent dipole magnetic field strengths of $B_* \sim 10^{15} \text{ G} - 10^{16} \text{ G}$ (Metzger et al. 2011) combined with $P_* \sim 1 \text{ ms} - 3 \text{ ms}$ and for SLSN (Kasen & Bildsten 2010; Chatzopoulos et al. 2016), lower $B_* \sim 10^{13} \text{ G} - 10^{14} \text{ G}$ magnetic fields combined with similar spin periods (though some SLSNe are fit by magnetars with magnetic fields approaching $B_* \sim 10^{15} \text{ G}$ and longer periods $P_* \gtrsim 10 \text{ ms}$, see

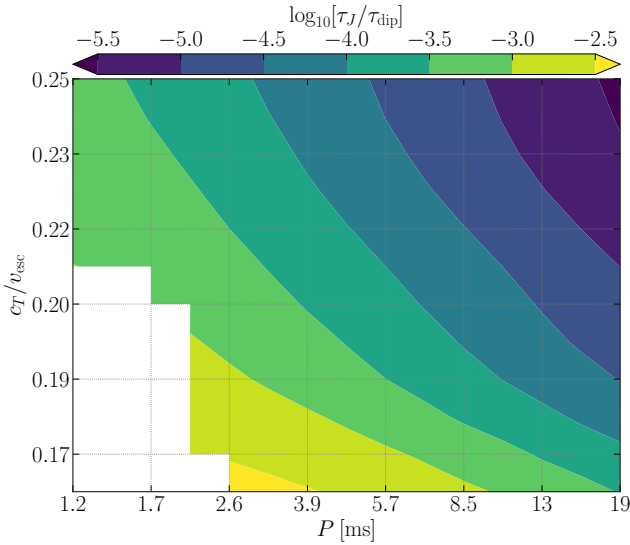


Figure 11. The ratio of the wind spindown time (Equation (35)) to the dipole spindown time (Equation (66)) as a function of sound speed and period, for fixed $B_* = 10^{15}$ G. For all simulations on our grid, $\tau_J \ll \tau_{\text{dip}}$.

Kasen & Bildsten 2010; Hsu et al. 2021). Typically in these models, the spindown is assumed to follow that of a force-free vacuum dipole model:

$$\tau_{\text{dip}} = \frac{E_{\text{rot}}}{2L_{\text{dip}}}, \quad (66)$$

where L_{dip} is the dipole luminosity:

$$L_{\text{dip}} = \frac{2R_*^6 B_*^2 \Omega_*^4}{3c^3} = \frac{2}{3} \sigma \dot{M} R_*^2 \Omega_*^2. \quad (67)$$

This assumption is appropriate after the flow becomes relativistic and Poynting-flux dominated. However, as discussed by Thompson et al. (2004); Metzger et al. (2007), in the early phase of proto-neutron star cooling, the flow is non-relativistic and the spindown timescale is much shorter than a naive application of the dipole expression would indicate. For example, the spindown time as approximated by Equation (57) for $B_* = 10^{15}$ G, $P_* = 19$ ms, and $\dot{M} = 10^{-4} M_{\odot} \text{ s}^{-1}$, indicates that the spindown time should be approximately $\tau_J \sim 6 \times 10^{-4} \tau_{\text{dip}}$. We show the ratio of the measured spindown time to the dipole spindown time for our full grid of 2D simulations in Figure 11. As expected, our wind-coupled spindown times are smaller than the dipole spindown times by many orders of magnitude.

One implication of this is that the initial rotation speed of the proto-magnetar must be in excess of the rotation speeds assumed by the dipole spindown models. Otherwise, the enhanced wind-coupled spindown would reduce the rotation rate to the point where the magnetar could not enhance the late-time luminosity of the supernova. As an example, we can consider the case of the SLSN ASASSN 15lh (Dong et al. 2016), which is inferred from lightcurve modeling⁶ (Chatzopoulos et al. 2016; Li et al. 2020) to be powered by a magnetar with $B_* \sim 10^{13}$ G– 10^{14} G and $P_* \simeq 1$ ms. Such a neutron star would have had a spindown timescale of $\tau_{\text{dip}} \sim 10$ d – 400 d, assuming dipole spindown. Using the analytic scalings developed in the previous section, we can scale our measured spindown times to

the lower values B_* inferred from SLSN models; in doing so we find wind-coupled spindown timescales ranging from $\tau_J \sim 29.0$ s – 183 s at the highest c_T , to $\tau_J \sim 61.5$ s – 388 s at the lowest c_T .

Furthermore, our models produce substantial energy loss rates, well in excess of 10^{51} ergs s^{-1} for millisecond rotators (see Figure 2c). As the cooling epoch lasts 1 s – 30 s (increasing with decreasing c_T), this would contribute a substantial amount of energy to the supernova explosion itself, even for magnetars with spindown times longer than the cooling epoch. While scaling B_* down to the magnitudes associated with SLSNe (10^{13} G to 10^{15} G) significantly reduces the wind power, at least for the more magnetic SLSNe models, it does not completely eliminate the total wind energy loss as a significant contribution to the total explosion energy. We can approximate the energy loss rate as:

$$\dot{E} \sim \dot{M} v_M^2. \quad (68)$$

For small B_* , the magnetic field adopts a split-monopole configuration and \dot{M} is nearly independent of B_* . We also have $v_M^2 \sim \sigma^{2/3} \sim B_*^{4/3}$. Thus, the energy loss rate should scale as

$$\dot{E} \sim B_*^{4/3} \quad (69)$$

Scaling our models by this factor, we find that a ASASSN-15lh-like magnetar with $B_* \sim 10^{14}$ G and $P_* \sim 1$ ms would carry a total wind energy $E_w \sim 10^{50}$ ergs during the cooling epoch, about 0.1 percent of the total explosion energy (Li et al. 2020). However, a more magnetized model, such as the magnetar powering DES14C1rhg (Hsu et al. 2021) with $B_* \sim 7 \times 10^{14}$ G and $P_* \sim 13$ ms can have an energy loss rate as large as $\dot{E} \sim 5 \times 10^{51}$ ergs s^{-1} (accounting for the B_* scaling), which even if sustained for 1 s would exceed the kinetic energy of the ejecta.

An important note is that our simulations do not capture all of important physics in the proto-neutron star wind problem. In particular, we do not include neutrino heating/cooling or a detailed electron/positron equation of state (but see Prasanna et al. 2022). The mapping between our results and the full problem is thus imperfect. In addition, as discussed by Thompson et al. (2004); Bucciantini et al. (2006); Metzger (2009), the flow rapidly becomes relativistic and Poynting-flux dominated, implying that relativistic calculations are necessary to capture the dynamics as the flow transitions to the relativistic regime. Such calculations are readily performed in Athena++, and will be explored in future papers on this topic.

4.3 Other Applications

In addition to proto-magnetar winds, we also scale to regimes representative of Sun-like stars and irradiated hot Jupiters. Using these scalings, we can apply the simulations discussed in this paper to these systems. We can also apply the analytic estimates developed in the previous section to these other contexts. See Table 1 and Appendix C for more information on our unit scalings.

4.3.1 Sun-like Stars

Low-mass main sequence stars are magnetically active and drive outflows. Indeed, the original Parker wind model (Parker 1958) was developed to describe our own Sun’s wind. Understanding the magnetocentrifugal braking mechanism in these stars is crucial to understanding and modeling the spindown evolution of these stars. While our models do not capture the more complex field geometries seen in the Sun and similar stars (DeRosa et al. 2012; Saikia et al. 2016; Finley & Matt 2017, 2018), they still provide a useful starting

⁶ Including interactions with the circumstellar medium.

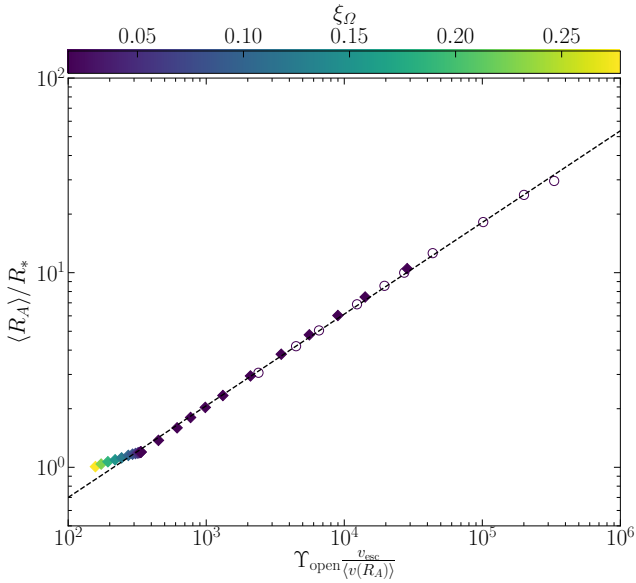


Figure 12. The normalized average Alfvén radius $\langle R_A \rangle / R_*$ versus the wind magnetization, as measured in our simulations (diamonds) and as reported by Finley & Matt (2017) for their pure dipole model (open circles). Models are colored according to the dimensionless rotation rate ξ_Ω . The dashed line shows the fit to the FM17 data as discussed therein. We see that our simulations fall along this fit except at the highest rotation rates.

point for investigating the physics of these objects (and the dipole component of the field may be the most important for the wind structure and evolution, e.g., Finley & Matt 2017).

Finley & Matt (2017) (hereafter, FM17) consider polytropic wind models of sun-like stars with $\xi_\Omega = 6.307 \times 10^{-3}$ (a factor of ~ 3 smaller than the most slowly rotating model in our grid), $\xi_T = 0.25$ (at the surface), and a range of ξ_B from 0.1 to 24 (2 to 500 times larger than our fiducial ξ_B). The principal quantity they measure in their simulations is the average Alfvén radius (Equation 45), which they use as a measure of the normalized spindown torque. They find that this quantity is well-fit by a power law in the quantity

$$\Upsilon_{\text{open}} \frac{\langle v_A \rangle}{v_{\text{esc}}} \equiv \frac{\Phi_{\text{open}}^2}{\dot{M} R_*^2 v_{\text{esc}}} \frac{\langle v_A \rangle}{v_{\text{esc}}}, \quad (70)$$

where $\langle v_A \rangle$ is the average of the Alfvén velocity over all points on S_A .

In Figure 12, we plot our measurements of $\langle R_A \rangle$ compared to those of FM17. We compare a collection of slow rotators $\xi_\Omega = 6.447 \times 10^{-3}$ at varying ξ_B , with sound speed $\xi_T = 0.247$, to 10 pure dipole simulations from FM17. In addition, we also show the value of $\langle R_A \rangle$ for simulations of more rapid rotators with $\xi_B = 0.046$. We find that the slow rotators are well-fit by the empirical fit found in FM17⁷, but the rapid rotators quickly deviate from this relation. This is in line with the analytic expectations we developed in the previous section.

4.3.2 Hot Jupiters

Hot Jupiters with orbital and spin periods of order $P_* \sim 1$ d have plasma atmospheres ionized by the intense radiation of their host

stars. Models of these atmospheres (Murray-Clay et al. 2009) (hereafter, MC09) show that they drive outflows that are well modeled by an isothermal, Parker-type wind⁸ with $c_T \approx 10$ km s⁻¹. These planets should also have strong magnetic fields, though perhaps weaker than Jupiter’s field due to their slower rotation period. Though the influence of their host stars (through their gravity, radiation, and magnetic fields) will have a significant effect on the structure and evolution of these planets’ winds, our existing simulations can provide a useful point of comparison for this problem.

In Figure 13, we show the measured \dot{M} across a range of magnetic field strengths appropriate to the hot Jupiter regime ($B_* \sim 1$ G), for a warm ($c_T = 13$ km/sec) and cool ($c_T = 9$ km/sec) model, each with a period of $P_* = 96$ h. These values correspond to $\xi_B \sim 2.442, 0.7724$, $\xi_T = 0.2341, 0.3485$, $\xi_\Omega = 4.876 \times 10^{-2}$ in our dimensionless units. We find a range of \dot{M} , from as low as 7×10^9 g s⁻¹ at the largest B_* considered, to as high as 7×10^{10} g s⁻¹ at the shortest P_* considered. These values are similar to those found by MC09 for the lowest incident UV flux (e.g., their case of a hot Jupiter orbiting a sun-like main sequence star, which has $\dot{M} = 3.3 \times 10^{10}$ g s⁻¹). For larger UV fluxes, the effective sound speed of the wind increases, which causes the mass loss rate of the wind to increase exponentially (as in Equation 30). For their example of a hot Jupiter orbiting a T Tauri star, they use a sound speed of $c_T \approx 30$ km s⁻¹, and find a mass loss rate 200 times greater than with the main sequence star, (which is roughly the \dot{M} expected analytically for that c_T). It should be noted that these models are 1D and non-magnetic. At larger B ($B \gtrsim 10^{-1}$ G to 1 G, depending on c_T), magnetic confinement can significantly reduce the mass loss rate, as can be seen in Figure 13.

Owen & Adams (2014) perform 2D simulations including the effects of a magnetic field, but exclusively for high UV fluxes. Their measured mass loss rates are smaller than those found by MC09 by a factor of ~ 10 , though still larger than our values by nearly the same factor. Even were the higher UV fluxes accounted for, however, the Owen & Adams (2014) simulations show that the planet’s magnetic field is opened up by the host star’s magnetic field, leading to a significant difference in the mass loss rate between the day and night sides of the planet, an effect that cannot be captured in our simulations.

We also measure the spindown rates of the wind. While hot Jupiters are tidally locked to their host stars and cannot actually spin down, the spindown time can still be used to infer the relative strength of the torque the wind exerts on the planet. The fastest spindown time we measure is $\tau_J = 3.4 \times 10^9$ yr, for extremely fast rotation periods of $P = 14.5$ h. For more reasonable rotation periods, the spindown times exceed a Hubble time. From this, we can infer that the spindown torque caused by the wind is unlikely dynamically important for hot Jupiters, except possibly for anomalously fast rotators early in their evolution (i.e., before they have had time to become tidally locked).

5 CONCLUSIONS

We have presented results from a suite of non-relativistic two-dimensional MHD simulations exploring the mass loss and spindown rates of stars characterized by a range of rotation rates and sound speeds. Our simulations show the trends in \dot{M} , \dot{J} , and \dot{E} with

⁷ Itself following the semi-analytic solution developed in Pantolmos & Matt (2017).

⁸ Though their simulations also include tidal gravity.

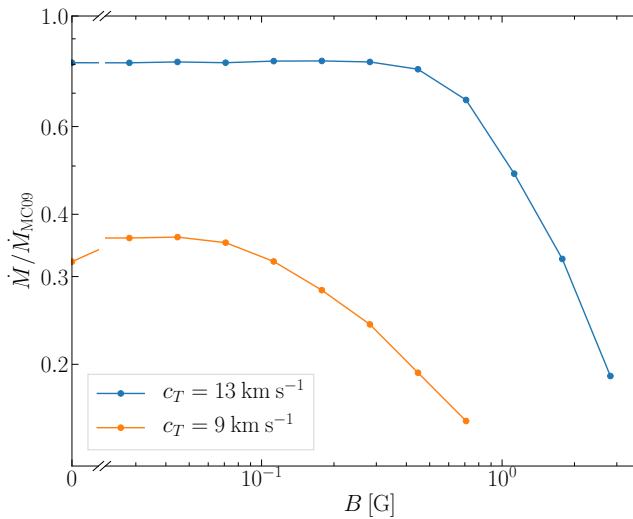


Figure 13. The mass loss rate, relative to the values in MC09 measured in our hot Jupiter models as a function of the magnetic field strength B . We show this for a hot (blue) and cool (orange) model, corresponding to the low and high F_{UV} models run by MC09. \dot{M} approaches a constant for small ξ_B in both cases, with a value a few times smaller than reported by MC09. We note that in both cases, maximum \dot{M} is achieved at $B > 0$; this is a consequence of the non-zero rotation rate of these simulations.

respect to the core rotation rate, isothermal sound speed, and magnetic field strength (Figure 2). We also investigate 3D simulations where the magnetosphere is tilted with respect to the axis of rotation (Figure 8). We also make discuss our simulations in the context of sun-like stars (Figure 12) and Hot Jupiters (Figure 13). We find our simulations to be in rough agreement with the existing literature on these topics (e.g., Finley & Matt 2017, 2018 and Murray-Clay et al. 2009; Owen & Adams 2014), though additional work to be done in order to make a more apposite comparison.

There are several targets for improvement we must make in order to improve the accuracy of our simulations in the proto-magnetar context. First, as discussed by Thompson et al. (2004), the wind velocity at the Alfvén point rapidly approaches c during the proto-neutron star cooling epoch and the flow becomes Poynting-flux dominated and relativistic. We also measure wind magnetizations $\sigma > 1$ in our most extreme simulations. For this reason, we need to include a treatment of relativistic MHD using the modules in Athena++. The other major improvements to be made are additional microphysics, realistic EOS (Coleman 2020), and neutrino heating and cooling. We have already begun this approach in Prasanna et al. (2022). With such improvements in play, we should be able to answer additional questions about the magnetar model of various astrophysical phenomena, including GRBs, SLSNe, and r -process nucleosynthesis in proto-magnetar winds. (Thompson & ud Doula 2018).

ACKNOWLEDGMENTS

We thank Jim Stone, Kengo Tomida, and Adam Finley, and Asif ud-Doula for helpful discussions. TAT thanks Brian Metzger, Niccolo Bucciantini, and Eliot Quataert for discussions and collaboration on this and related topics. TAT acknowledges support from a Simons Foundation Fellowship and an IBM Einstein Fellowship from the Institute for Advanced Study, Princeton. TAT and MJR

are supported in part by NASA grant 80NSSC20K0531. MC acknowledges support from the U. S. Department of Energy Office of Science and the Office of Advanced Scientific Computing Research via the Scientific Discovery through Advanced Computing (SciDAC4) program and Grant DE-SC0018297 (subaward 00009650) and support from the U. S. National Science Foundation (NSF) under Grants AST-1714267 and PHY-1804048 (the latter via the Max-Planck/Princeton Center (MPPC) for Plasma Physics).

DATA AVAILABILITY

The data underlying this article will be shared on reasonable request to the corresponding author.

REFERENCES

- Akiyama S., Wheeler J. C., Meier D. L., Lichtenstadt I., 2003, *ApJ*, 584, 954
- Blandford R. D., Payne D. G., 1982, *MNRAS*, 199, 883
- Bucciantini N., Thompson T. A., Arons J., Quataert E., Del Zanna L., 2006, *MNRAS*, 368, 1717
- Bucciantini N., Quataert E., Metzger B. D., Thompson T. A., Arons J., Del Zanna L., 2009, *MNRAS*, 396, 2038
- Burrows A., Hayes J., Fryxell B. A., 1995, *ApJ*, 450, 830
- Chatzopoulos E., Wheeler J. C., Vinko J., Nagy A. P., Wiggins B. K., Even W. P., 2016, *ApJ*, 828, 94
- Coleman M. S. B., 2020, *ApJS*, 248, 7
- Crank J., Nicolson P., 1947, *Mathematical Proceedings of the Cambridge Philosophical Society*, 43, 50–67
- DeRosa M. L., Brun A. S., Hoeksema J. T., 2012, *ApJ*, 757, 96
- Dong S., et al., 2016, *Science*, 351, 257
- Duncan R. C., Shapiro S. L., Wasserman I., 1986, *ApJ*, 309, 141
- Finley A. J., Matt S. P., 2017, *ApJ*, 845, 46
- Finley A. J., Matt S. P., 2018, *ApJ*, 854, 78
- Gressl C., Veronig A. M., Temmer M., Odstrčil D., Linker J. A., Mikić Z., Riley P., 2014, *Sol. Phys.*, 289, 1783
- Hoffman R. D., Woosley S. E., Qian Y. Z., 1997, *ApJ*, 482, 951
- Hsu B., Hosseinzadeh G., Berger E., 2021, arXiv e-prints, 2104, arXiv:2104.09639
- Janka H.-T., Müller E., 1995, *ApJ*, 448, L109
- Janka H. T., Müller E., 1996, *A&A*, 306, 167
- Kasen D., Bildsten L., 2010, *ApJ*, 717, 245
- Keppens R., Goedbloed J. P., 2000, *ApJ*, 530, 1036
- Komissarov S. S., Barkov M. V., 2007, *MNRAS*, 382, 1029
- Lamers H. J. G. L. M., Cassinelli J. P., 1999, *Introduction to Stellar Winds*. Cambridge University Press, <https://ui.adsabs.harvard.edu/abs/1999isw.book.....L>
- Li L., Dai Z.-G., Wang S.-Q., Zhong S.-Q., 2020, *ApJ*, 900, 121
- Lionello R., Linker J. A., Mikić Z., 2001, *ApJ*, 546, 542
- Lionello R., Linker J. A., Mikić Z., 2009, *ApJ*, 690, 902
- Mestel L., Spruit H. C., 1987, *MNRAS*, 226, 57
- Metzger B. D., 2009, PhD thesis, University of California, Berkeley, <https://ui.adsabs.harvard.edu/abs/2009PhDT.....19M>
- Metzger B. D., Thompson T. A., Quataert E., 2007, *ApJ*, 659, 561
- Metzger B. D., Giannios D., Thompson T. A., Bucciantini N., Quataert E., 2011, *MNRAS*, 413, 2031
- Michel F. C., 1969, *ApJ*, 158, 727
- Murray-Clay R. A., Chiang E. I., Murray N., 2009, *ApJ*, 693, 23
- Nishimura N., Sawai H., Takiwaki T., Yamada S., Thielemann F.-K., 2017, *ApJ*, 836, L21
- Ostriker J. P., Gunn J. E., 1971, *ApJ*, 164, L95
- Otsuki K., Tagoshi H., Kajino T., ya Wanajo S., 2000, *ApJ*, 533, 424
- Owen J. E., Adams F. C., 2014, *MNRAS*, 444, 3761
- Pantolmos G., Matt S. P., 2017, *ApJ*, 849, 83
- Parker E. N., 1958, *ApJ*, 128, 664

- Prasanna T., Coleman M. S. B., Raives M. J., Thompson T. A., 2022, *MNRAS*, 517, 3008
- Qian Y. Z., Woosley S. E., 1996, *ApJ*, 471, 331
- Reiss M. A., Temmer M., Veronig A. M., Nikolic L., Vennerstrom S., Schön-gassner F., Hofmeister S. J., 2016, *Space Weather*, 14, 495
- Saikia S. B., et al., 2016, *A&A*, 594, A29
- Sakurai T., 1985, *A&A*, 152, 121
- Schatzman E., 1962, *Annales d'Astrophysique*, 25, 18
- Stone J. M., Tomida K., White C., Felker K. G., 2019, *Athena++: Radiation GR magnetohydrodynamics code (ascl:1912.005)*, <https://ui.adsabs.harvard.edu/abs/2019ascl.soft12005S>
- Subramanian S., Balsara D. S., ud Doula A., Gagné M., 2022, *MNRAS*, 515, 237
- Suess S. T., Richter A. K., Winge C. R., Nerney S. F., 1977, *ApJ*, 217, 296
- Suess S. T., Wang A. H., Wu S. T., Poletto G., McComas D. J., 1999, *J. Geophys. Res.*, 104, 4697
- Sukhbold T., Thompson T. A., 2017, *MNRAS*, 472, 224
- Symbalisty E. M. D., 1984, *ApJ*, 285, 729
- Thompson T. A., 2003, *ApJ*, 585, L33
- Thompson T. A., 2007, in *Revista Mexicana de Astronomia y Astrofisica*, vol. 27, pp 80–90 ([arXiv:astro-ph/0611368](https://arxiv.org/abs/astro-ph/0611368))
- Thompson C., Murray N., 2001, *ApJ*, 560, 339
- Thompson T. A., ud Doula A., 2018, *MNRAS*, 476, 5502
- Thompson T. A., Burrows A., Meyer B. S., 2001, *ApJ*, 562, 887
- Thompson T. A., Burrows A., Pinto P. A., 2003, *ApJ*, 592, 434
- Thompson T. A., Chang P., Quataert E., 2004, *ApJ*, 611, 380
- Thompson T. A., Quataert E., Burrows A., 2005, *ApJ*, 620, 861
- Vidotto A. A., 2009, PhD thesis, IAG - Universidade de Sao Paulo (Brazil), <https://ui.adsabs.harvard.edu/abs/2009PhDT.....94V>
- Vidotto A. A., Jardine M., Morin J., Donati J. F., Opher M., Gombosi T. I., 2014, *MNRAS*, 438, 1162
- Vurm I., Metzger B. D., 2021, *arXiv e-prints*, p. arXiv:2101.05299
- Wanajo S., Kajino T., Mathews G. J., Otsuki K., 2001, *ApJ*, 554, 578
- Weber E. J., Davis Jr. L., 1967, *ApJ*, 148, 217
- Wheeler J. C., Yi I., Höflich P., Wang L., 2000, *ApJ*, 537, 810
- Woosley S. E., 2010, *ApJ*, 719, L204
- Woosley S. E., Wilson J. R., Mathews G. J., Hoffman R. D., Meyer B. S., 1994, *ApJ*, 433, 229
- ud Doula A., Owocki S. P., 2002, *ApJ*, 576, 413
- van Saders J. L., Ceillier T., Metcalfe T. S., Silva Aguirre V., Pinsonneault M. H., García R. A., Mathur S., Davies G. R., 2016, *Nature*, 529, 181

APPENDIX A: ROTATING REFERENCE FRAME

Consider a rotating reference frame, which rotates with respect to the inertial, laboratory frame at a constant angular velocity Ω_* . The coordinates transform between the (primed) rotating frame and the (unprimed) inertial frame according to:

$$r \rightarrow r' \quad (\text{A1})$$

$$\theta \rightarrow \theta' \quad (\text{A2})$$

$$\phi \rightarrow \phi' + \Omega_* t'. \quad (\text{A3})$$

In addition to the coordinates, the velocity and magnetic fields differ between the reference frames. They transform as:

$$\mathbf{v} \rightarrow \mathbf{v}' + \Omega_* \times \mathbf{r}' \quad (\text{A4})$$

$$\mathbf{B} \rightarrow \mathbf{B}'. \quad (\text{A5})$$

Although only ϕ' and \mathbf{v}' differ from their inertial counterparts, we will still be explicit with our use of primes throughout these appendices to make it clear exactly when we are working in the rotating frame.

A1 Coriolis and Centrifugal Forces

The motion of a particle in a rotating reference frame behaves as if acted on by the “fictitious” Coriolis

$$\mathbf{F}'_{\text{cor}} \equiv \left. \frac{\partial \rho \mathbf{v}'}{\partial t'} \right|_{\text{cor}} = -2\Omega_* \times \rho \mathbf{v}' \quad (\text{A6})$$

and centrifugal

$$\mathbf{F}'_{\text{cen}} \equiv \left. \frac{\partial \rho \mathbf{v}'}{\partial t'} \right|_{\text{cen}} = -\Omega_* \times \rho (\Omega_* \times \mathbf{r}') \quad (\text{A7})$$

forces. In the code, these are implemented as additional source terms. In principle, the centrifugal force is straightforward:

$$\mathbf{F}'_{\text{cen}} = r' \rho \Omega_*^2 \sin \theta' (\hat{\mathbf{r}} \sin \theta' + \hat{\boldsymbol{\theta}} \cos \theta'). \quad (\text{A8})$$

However, to achieve better accuracy, we take the average of the centrifugal force term over the cell:

$$\langle \mathbf{F}'_{\text{cen}} \rangle = \frac{\rho \Omega_*^2 \partial \phi}{\partial V} \int_{r_i}^{r_{i+1}} \int_{\theta_j}^{\theta_{j+1}} (r')^2 \sin \theta' \mathbf{F}'_{\text{cen}} dr' d\theta', \quad (\text{A9})$$

where ∂V is the cell volume and $\partial \phi$ is the cell width. This leads to a velocity source term

$$\partial \rho \mathbf{v}'_{\text{cen}} = \langle \mathbf{F}'_{\text{cen}} \rangle \partial t' \quad (\text{A10})$$

$$\partial \rho \mathbf{v}'_{\text{cen}} = \Xi \begin{pmatrix} -9\Delta_1 [\cos \theta'] - \Delta_1 [\cos(3\theta')] \\ 4\Delta_3 [\sin \theta] \\ 0 \end{pmatrix} \quad (\text{A11})$$

where $\partial t'$ is the timestep,

$$\Xi \equiv \frac{\rho \Omega_* \Delta_4 [r] \partial \phi \partial \psi'}{48 \partial V}, \quad (\text{A12})$$

$$\partial \psi' \equiv \Omega_* \partial t', \quad (\text{A13})$$

and we define

$$\Delta_a [f] \equiv f_{i+1}^a - f_i^a \quad (\text{A14})$$

for some quantity f across cell faces i and $i + 1$.

When implementing the Coriolis force, we must update the momenta⁹ semi-implicitly (Crank & Nicolson 1947) in order to conserve energy:

$$\rho \mathbf{v}'_{\text{new}} = \partial \psi' \frac{\mathbf{F}'_{\text{new}} + \mathbf{F}'_{\text{old}}}{2} + \rho \mathbf{v}'_{\text{old}}, \quad (\text{A15})$$

where \mathbf{F}' here is the Coriolis force. Solving this implicit equation, we find that the Coriolis source term is

$$\partial \rho \mathbf{v}'_{\text{cor}} = \frac{\partial \psi' (\rho \mathbf{u}'_{\text{cor}} - 2\hat{\mathbf{z}} \times \rho \mathbf{v}') - (\partial \psi')^2 \rho \mathbf{v}'}{1 + (\partial \psi')^2}, \quad (\text{A16})$$

where

$$\rho \mathbf{u}'_{\text{cor}} = \rho \partial \psi' \begin{pmatrix} v'_r \cos(2\theta') - v'_\theta \sin(2\theta') \\ -v'_r \sin(2\theta') - v'_\theta \cos(2\theta') \\ -v'_\phi \end{pmatrix}. \quad (\text{A17})$$

⁹ Though ρ remains constant through this step.

APPENDIX B: VECTOR POTENTIAL FOR A TILTED DIPOLE

The initial conditions for the magnetic field we impose are that of a tilted dipole. Since we must specify this by its vector potential, we derive the form of that potential here. The vector potential of a magnetic dipole is

$$\mathbf{A}' = \frac{\mathbf{m}' \times \mathbf{r}'}{r'^3}. \quad (\text{B1})$$

Let the magnetic moment \mathbf{m}' be a vector of magnitude $m' = \frac{1}{2} B'_* R_*^3$, tilted with respect to $\boldsymbol{\Omega}$ by some angle α . By convention, we choose the plane defined by those two vectors to be the $\phi' = 0$ plane (in Cartesian coordinates, the x' - z plane). The components of the vector potential are then:

$$\mathbf{A}' = \frac{B'_* R_*^3}{2 r'^2} \begin{pmatrix} 0 \\ -\sin \alpha \sin \phi' \\ \cos \alpha \sin \theta' - \cos \theta' \cos \phi' \sin \alpha \end{pmatrix} \quad (\text{B2})$$

We choose the magnitude to be defined by $B'_*/2$ rather than B'_* so that the magnitude of the magnetic field at the magnetic pole is

$$B'_p = \mathbf{B}' \cdot \mathbf{B}'|_{r'=R_*, \theta'=\alpha, \phi'=0} = B'_*. \quad (\text{B3})$$

APPENDIX C: UNITS

When we initialize our simulations in hydrostatic equilibrium, we choose to normalize the density profile such that $\rho_* = GM_* = R_* = 1$. These three quantities form a basis over the basic kinematic units of length, mass, and time.¹⁰ They, in effect, define a set of dimensionless “code units” that can be converted back to physical units only after choosing a physical scale, i.e., choosing values of ρ_* , GM_* , and R_* in some physical unit system. This means that we can freely change the scale of our simulations without repeating them, simply by choosing the appropriate scale factors, which are given by

$$L = R_* \quad (\text{C1})$$

$$M = \rho_* R_*^3 \quad (\text{C2})$$

$$T = \sqrt{\frac{R_*^3}{GM_*}}. \quad (\text{C3})$$

For instance, to convert, e.g., the simulation velocity output into physical units, you would multiply the velocity by a factor of $LT^{-1} = \sqrt{GM_*/R_*}$, with appropriate M_* and R_* to the problem of interest. The choice of scales used in this paper are summarized in Table 1.

APPENDIX D: BOUNDARY CONDITIONS

D1 Inner Boundary

We wish to enforce boundary conditions on the inner boundary such that we maintain

$$\frac{\partial B'_{r'}}{\partial t'} = 0 \quad (\text{D1})$$

¹⁰ And, in cgs units, electromagnetic quantities are measured in these kinematic units.

without directly setting the magnetic field components. We accomplish this as follows. First, consider, from Maxwell’s equations:

$$\frac{\partial \mathbf{B}'}{\partial t'} = -c \nabla' \times \mathbf{E}' \quad (\text{D2})$$

$$\frac{\partial B'_{r'}}{\partial t'} = -\frac{c}{r' \sin \theta'} \left(\frac{\partial}{\partial \theta} (E'_{\phi'} \sin \theta') - \frac{\partial E'_{\theta'}}{\partial \phi'} \right). \quad (\text{D3})$$

In the special case of *aligned* rotation (i.e., where $\mathbf{m}' \cdot \boldsymbol{\Omega} = 0$), all $\frac{\partial}{\partial \phi'}$ terms vanish and fixing $E'_{\phi'} = 0$ is sufficient to prevent anomalous growth of the magnetic field. However, once the magnetosphere is tilted with respect to the rotational axis, azimuthal symmetry can no longer be assumed, and we must fix both $E'_{\phi'} = 0$ and $E'_{\theta'} = 0$ in order to achieve our stated goals.

D2 Outer Boundary

At the outer boundary, we wish to enforce:

$$\dot{M} = \text{const}, \quad \rho = \text{const}, \quad \mathbf{L}' = \text{const}, \quad \mathbf{B}' = \text{const}, \quad (\text{D4})$$

Where $\boldsymbol{\tau}'$ is the torque. This comprises 7 constraints ($\mathbf{L}' \cdot \mathbf{r}' = 0$ by definition, and thus provides no constraint), sufficient to fix the 3 components each of \mathbf{v}' and \mathbf{B}' , as well as ρ . The constraints on ρ and \mathbf{B}' are self explanatory, but some work must be done to turn these constraints into direct constraints of the components of \mathbf{v}' . The constraint on \dot{M} and that on ρ together give us a constraint on v'_r :

$$v'_r|_{\text{gh}} = v'_r|_{\text{outer}} \left(\frac{r'_{\text{outer}}}{r'_{\text{gh}}} \right)^2 \quad (\text{D5})$$

where “gh” indicates quantities in the ghost zone and “outer” indicates quantities in the last outer active cell. From the angular momentum constraint, we obtain:

$$v'_{\theta}|_{\text{gh}} = v'_{\theta}|_{\text{outer}} \frac{r'_{\text{outer}}}{r'_{\text{gh}}} \quad (\text{D6})$$

$$v'_{\phi}|_{\text{gh}} = v'_{\phi}|_{\text{outer}} \frac{r'_{\text{outer}}}{r'_{\text{gh}}} + \Omega_* \left(\frac{r'^2_{\text{outer}} - r'^2_{\text{gh}}}{r_{\text{gh}}} \right). \quad (\text{D7})$$

APPENDIX E: FULL TABLE OF RESULTS

In this section we present a full table of wind properties for the simulations presented in Section 3. All simulations presented here have $\xi_B = 0.046$ and values are scaled as:

$$\dot{M} \equiv \dot{M}/4\pi R_*^2 \rho_0 c_T = \dot{M}/\dot{M}_0 \quad (\text{E1})$$

$$\dot{J} \equiv \dot{J}/\dot{M}_0 R_*^2 \Omega_* \quad (\text{E2})$$

$$\dot{E} \equiv \dot{E}/\dot{M}_0 c_T^2 \quad (\text{E3})$$

$$\tau_J \equiv \tau_J/(R_* c_T^{-1}). \quad (\text{E4})$$

ξ_T	ξ_Ω	$\log_{10} \dot{M}$	$\log_{10} \dot{J}$	$\log_{10} \dot{E}$	$\log_{10} \tau_J$	Φ/Φ_0	ξ_T	ξ_Ω	$\log_{10} \dot{M}$	$\log_{10} \dot{J}$	$\log_{10} \dot{E}$	$\log_{10} \tau_J$	Φ/Φ_0		
0.247	0.278	-1.4008	-1.3939	-0.5419	4.3416	0.9758	0.217	0.278	-1.8019	-1.5857	-0.8756	4.5333	0.8184		
	0.228	-1.4700	-1.4368	-0.5965	4.3845	0.9564		0.228	-1.9627	-1.6959	-1.0129	4.6435	0.8015		
	0.187	-1.5273	-1.4703	-0.6427	4.4179	0.9481		0.187	-2.0957	-1.7772	-1.1278	4.7248	0.7998		
	0.153	-1.5718	-1.4946	-0.6789	4.4423	0.9523		0.153	-2.1983	-1.8289	-1.2165	4.7765	0.7998		
	0.126	-1.6050	-1.5080	-0.7060	4.4556	0.9616		0.126	-2.2778	-1.8548	-1.2853	4.8024	0.8083		
	0.103	-1.6283	-1.5058	-0.7252	4.4534	0.9898		0.103	-2.3408	-1.8711	-1.3398	4.8187	0.8167		
	0.085	-1.6465	-1.5117	-0.7402	4.4593	0.9968		0.085	-2.3897	-1.8782	-1.3819	4.8258	0.8228		
	0.069	-1.6598	-1.5182	-0.7510	4.4658	0.9967		0.069	-2.4280	-1.8874	-1.4148	4.8350	0.8186		
	0.057	-1.6690	-1.5224	-0.7586	4.4700	0.9979		0.057	-2.4564	-1.8935	-1.4392	4.8411	0.8144		
	0.047	-1.6754	-1.5257	-0.7639	4.4733	0.9989		0.047	-2.4769	-1.8957	-1.4567	4.8433	0.8135		
	0.038	-1.6797	-1.5275	-0.7674	4.4751	0.9992		0.038	-2.4916	-1.8979	-1.4692	4.8455	0.8111		
	0.031	-1.6827	-1.5284	-0.7699	4.4761	0.9990		0.031	-2.5020	-1.8992	-1.4780	4.8468	0.8094		
	0.026	-1.6847	-1.5291	-0.7716	4.4767	0.9994		0.026	-2.5091	-1.9003	-1.4841	4.8479	0.8078		
	0.021	-1.6861	-1.5295	-0.7727	4.4771	0.9996		0.021	-2.5140	-1.9011	-1.4883	4.8487	0.8065		
	0.017	-1.6870	-1.5297	-0.7734	4.4774	0.9998		0.017	-2.5174	-1.9017	-1.4912	4.8493	0.8055		
	0.240	0.278	-1.4983	-1.4626	-0.6136	4.4103		0.9370	0.210	0.278	-1.9209	-1.6556	-0.9788	4.6032	0.7845
		0.228	-1.5800	-1.4863	-0.6872	4.4339		0.9196		0.228	-2.1118	-1.7905	-1.1446	4.7382	0.7693
0.187		-1.6540	-1.5326	-0.7480	4.4802	0.9100	0.187	-2.2638		-1.8780	-1.2768	4.8256	0.7589		
0.153		-1.7108	-1.5655	-0.7951	4.5131	0.9121	0.153	-2.3850		-1.9346	-1.3829	4.8822	0.7644		
0.126		-1.7530	-1.5815	-0.8303	4.5291	0.9244	0.126	-2.4820		-1.9698	-1.4677	4.9175	0.7608		
0.103		-1.7832	-1.5806	-0.8556	4.5282	0.9534	0.103	-2.5603		-1.9915	-1.5359	4.9391	0.7628		
0.085		-1.8060	-1.5785	-0.8746	4.5261	0.9747	0.085	-2.6228		-2.0049	-1.5902	4.9525	0.7604		
0.069		-1.8231	-1.5780	-0.8889	4.5256	0.9870	0.069	-2.6722		-2.0170	-1.6328	4.9646	0.7526		
0.057		-1.8355	-1.5783	-0.8993	4.5259	0.9949	0.057	-2.7097		-2.0261	-1.6651	4.9737	0.7448		
0.047		-1.8443	-1.5801	-0.9066	4.5277	0.9965	0.047	-2.7371		-2.0304	-1.6886	4.9780	0.7402		
0.038		-1.8505	-1.5818	-0.9117	4.5295	0.9974	0.038	-2.7571		-2.0356	-1.7057	4.9832	0.7336		
0.031		-1.8547	-1.5828	-0.9152	4.5304	0.9984	0.031	-2.7713		-2.0403	-1.7178	4.9879	0.7274		
0.026		-1.8576	-1.5834	-0.9176	4.5311	0.9986	0.026	-2.7812		-2.0460	-1.7263	4.9936	0.7200		
0.021		-1.8595	-1.5838	-0.9193	4.5314	0.9989	0.021	-2.7880		-2.0510	-1.7321	4.9986	0.7135		
0.017		-1.8608	-1.5840	-0.9204	4.5316	0.9990	0.017	-2.7927		-2.0549	-1.7360	5.0025	0.7086		
0.232		0.278	-1.5902	-1.4833	-0.6932	4.4309	0.9121	0.202		0.187	-2.4319	-1.9712	-1.4350	4.9188	0.7389
		0.228	-1.7000	-1.5472	-0.7876	4.4948	0.8818			0.153	-2.5774	-2.0382	-1.5623	4.9858	0.7378
	0.187	-1.7916	-1.6074	-0.8643	4.5550	0.8710	0.126		-2.7009	-2.0912	-1.6698	5.0388	0.7275		
	0.153	-1.8624	-1.6457	-0.9240	4.5933	0.8764	0.103		-2.7978	-2.1175	-1.7541	5.0651	0.7230		
	0.126	-1.9135	-1.6600	-0.9673	4.6076	0.8956	0.085		-2.8746	-2.1320	-1.8193	5.0796	0.7108		
	0.103	-1.9526	-1.6640	-1.0004	4.6117	0.9165	0.069		-2.9378	-2.1426	-1.8741	5.0903	0.7066		
	0.085	-1.9826	-1.6660	-1.0258	4.6136	0.9314	0.057		-2.9873	-2.1503	-1.9167	5.0979	0.6994		
	0.069	-2.0048	-1.6641	-1.0445	4.6118	0.9460	0.047		-3.0249	-2.1568	-1.9489	5.1044	0.6940		
	0.057	-2.0210	-1.6618	-1.0583	4.6094	0.9561	0.038		-3.0522	-2.1583	-1.9722	5.1059	0.6920		
	0.047	-2.0327	-1.6589	-1.0681	4.6065	0.9656	0.031		-3.0720	-2.1607	-1.9890	5.1083	0.6882		
	0.038	-2.0410	-1.6571	-1.0751	4.6047	0.9712	0.026		-3.0861	-2.1631	-2.0009	5.1107	0.6841		
	0.031	-2.0467	-1.6550	-1.0799	4.6027	0.9762	0.021		-3.0958	-2.1643	-2.0092	5.1119	0.6818		
	0.026	-2.0507	-1.6532	-1.0832	4.6008	0.9806	0.017		-3.1025	-2.1635	-2.0148	5.1111	0.6821		
	0.021	-2.0534	-1.6509	-1.0855	4.5986	0.9849	0.194		0.153	-2.7913	-2.1642	-1.7616	5.1118	0.6910	
	0.017	-2.0552	-1.6497	-1.0870	4.5973	0.9879			0.126	-2.9336	-2.2175	-1.8871	5.1651	0.6835	
	0.225	0.278	-1.6915	-1.5248	-0.7819	4.4724			0.8616	0.103	-3.0529	-2.2534	-1.9917	5.2010	0.6694
		0.228	-1.8270	-1.6172	-0.8957	4.5648			0.8390	0.085	-3.1531	-2.2865	-2.0769	5.2341	0.6424
0.187		-1.9400	-1.6916	-0.9917	4.6392	0.8315		0.069	-3.2334	-2.3004	-2.1469	5.2480	0.6361		
0.153		-2.0249	-1.7334	-1.0643	4.6810	0.8401		0.057	-3.2967	-2.3045	-2.2016	5.2521	0.6357		
0.126		-2.0886	-1.7532	-1.1190	4.7008	0.8514		0.047	-3.3459	-2.3070	-2.2437	5.2547	0.6337		
0.103		-2.1385	-1.7625	-1.1617	4.7101	0.8666		0.038	-3.3829	-2.3036	-2.2751	5.2513	0.6362		
0.085		-2.1766	-1.7638	-1.1943	4.7114	0.8814		0.031	-3.4101	-2.3014	-2.2980	5.2490	0.6381		
0.069		-2.2056	-1.7640	-1.2191	4.7116	0.8922		0.026	-3.4297	-2.2979	-2.3144	5.2455	0.6394		
0.057		-2.2274	-1.7657	-1.2376	4.7133	0.8970		0.021	-3.4436	-2.2960	-2.3260	5.2436	0.6410		
0.047		-2.2431	-1.7664	-1.2509	4.7140	0.8995		0.017	-3.4534	-2.2912	-2.3341	5.2388	0.6428		
0.038		-2.2541	-1.7655	-1.2603	4.7131	0.9034									
0.031		-2.2618	-1.7641	-1.2668	4.7117	0.9070									
0.026		-2.2671	-1.7629	-1.2713	4.7105	0.9098									
0.021		-2.2708	-1.7619	-1.2744	4.7095	0.9118									
0.017		-2.2733	-1.7612	-1.2765	4.7088	0.9132									

Table E1. (continued)

Table E1. Table of wind properties for all simulations considered in Section 3.

ξ_T	ξ_Ω	$\log_{10} \dot{M}$	$\log_{10} \dot{J}$	$\log_{10} \dot{E}$	$\log_{10} \tau_J$	Φ/Φ_0	
0.187	0.153	-3.0154	-2.2921	-1.9778	5.2397	0.6572	
	0.126	-3.1818	-2.3518	-2.1266	5.2994	0.6388	
	0.103	-3.3311	-2.4062	-2.2582	5.3538	0.6118	
	0.085	-3.4549	-2.4463	-2.3643	5.3939	0.5861	
	0.069	-3.5556	-2.4601	-2.4526	5.4077	0.5830	
	0.057	-3.6400	-2.4775	-2.5246	5.4251	0.5683	
	0.047	-3.7053	-2.4855	-2.5799	5.4332	0.5626	
	0.038	-3.7546	-2.4819	-2.6212	5.4295	0.5644	
	0.031	-3.7920	-2.4811	-2.6521	5.4287	0.5612	
	0.026	-3.8195	-2.4851	-2.6745	5.4328	0.5545	
	0.021	-3.8392	-2.4899	-2.6903	5.4375	0.5473	
	0.017	-3.8529	-2.4913	-2.7013	5.4390	0.5443	
	0.179	0.153	-3.2555	-2.4330	-2.2185	5.3806	0.6145
		0.126	-3.4635	-2.5247	-2.4065	5.4723	0.5729
0.103		-3.6463	-2.5974	-2.5693	5.5450	0.5380	
0.085		-3.8020	-2.6629	-2.7023	5.6105	0.4982	
0.069		-3.9330	-2.7091	-2.8149	5.6567	0.4711	
0.057		-4.0366	-2.7324	-2.9030	5.6800	0.4566	
0.047		-4.1173	-2.7413	-2.9706	5.6889	0.4481	
0.038		-4.1793	-2.7352	-3.0222	5.6828	0.4491	
0.031		-4.2283	-2.7409	-3.0617	5.6885	0.4428	
0.026		-4.2649	-2.7511	-3.0905	5.6987	0.4333	
0.021		-4.2909	-2.7465	-3.1110	5.6941	0.4321	
0.017		-4.3098	-2.7496	-3.1258	5.6973	0.4284	
0.172		0.126	-3.7759	-2.7147	-2.7369	5.6623	0.5047
		0.103	-3.9985	-2.8054	-2.9390	5.7531	0.4628
	0.085	-4.1891	-2.8879	-3.1026	5.8356	0.4246	
	0.069	-4.3525	-2.9470	-3.2409	5.8946	0.3903	
	0.057	-4.4890	-3.0051	-3.3516	5.9527	0.3632	
	0.047	-4.5967	-3.0478	-3.4369	5.9954	0.3376	
	0.038	-4.6756	-3.0705	-3.4983	6.0181	0.3287	
	0.031	-4.7373	-3.0891	-3.5456	6.0367	0.3168	
	0.026	-4.7788	-3.0734	-3.5777	6.0210	0.3192	
	0.021	-4.8118	-3.0704	-3.6023	6.0180	0.3149	
	0.017	-4.8377	-3.0876	-3.6213	6.0352	0.3044	
	0.164	0.085	-4.6305	-3.1035	-3.6377	6.0511	0.3761
		0.069	-4.8374	-3.1924	-3.8040	6.1400	0.3436
		0.057	-5.0101	-3.2651	-3.9304	6.2127	0.3119
0.047		-5.1437	-3.3119	-4.0220	6.2595	0.2863	
0.038		-5.2491	-3.3484	-4.0912	6.2960	0.2669	
0.031		-5.3365	-3.3888	-4.1479	6.3364	0.2502	
0.026		-5.3972	-3.4134	-4.1853	6.3611	0.2401	
0.021		-5.4495	-3.4452	-4.2195	6.3928	0.2263	
0.017		-5.4668	-3.4253	-4.2253	6.3729	0.2259	

Table E1. (continued)

This paper has been typeset from a $\text{\TeX}/\text{\LaTeX}$ file prepared by the author.